This is to certify that the
thesis entitled

PRELIMINARY INVESTIGATION OF THE FIRST
GENERATION INTERNAL COMBUSTION WAVE DISC
ENGINE

presented by

KANISHKA SHARMA

has been accepted towards fulfillment
of the requirements for the

M.S degree in MECHANICAL ENGINEERING

Major Professor's Signature

05/08/08

Date

PRELIMINARY DESIGN APPROACH TO THE FIRST GENERATION INTERNAL COMBUSTION WAVE DISC ENGINE

By

Kanishka Sharma

A THESIS

Submitted to
Michigan State University
in partial fulfillment of the requirements
for the degree of

MASTER OF SCIENCE

Department of Mechanical Engineering

2008

ABSTRACT

PRELIMINARY DESIGN APPROACH FOR THE FIRST GENERATION INTERNAL COMBUSTION WAVE DISC ENGINE

by

Kanishka Sharma

For the past decade the miniaturization of power generation devices has been a fascinating research topic. With the available micro fabrication methods and high specific energy of the hydrocarbon fuels, it gives us a compelling reason to explore and develop the possibilities of using such fuels for 'power generation on a chip. The Internal Combustion Wave Disc Engine (IC WDE) is one such concept. It is an unsteady flow device using energy exchanges via waves. The waves travel in channels which are arranged inside the disc, to extract work, to propel the disc, and to produce torque. The first part of the work discusses the working principle of the WDE and the gas dynamic relations that are used later to establish the gas dynamic model of the wave disc engine. Challenges of micro combustion are also presented. The second part of the work involves numerical simulations of an axial wave rotor that has been successfully commercialized as COMPREX® and can be seen as a predecessor among the unsteady flow devices. FLUENT® is used for these simulations and results are compared with a 1 D algebraic code developed and being used to design wave rotor porting and how to employ the same approach for the modeling of a WDE. In the third part of this work, supporting experimental work is presented that covers flow studies inside 4 different microchannels machined in a Si wafer. Friction factor are determined and compared with the available data from the literature.

To my family and friends

ACKNOWLEDGEMENTS

I would like to express my sincere and deepest gratitude to Prof. Norbert Müller for giving me this opportunity to work on this research project and make it an enriching learning experience. I would like to thank him for the independence he allowed me to explore different directions in this project, his guidance, motivation and his very positive outlook which really helped me enjoy this work. I am really honored and consider myself very lucky to have him as my advisor, mentor and a friend.

I would also like to express my sincere thanks to committee members Prof. I.S.Wichman and Prof. Guy Raguin for their very valuable suggestions and patience without which this work would not have been complete. I am particularly thankful to Dr Wichman for giving me an opportunity to perform my graduate studies at Michigan State University where I arrived in fall of 2005.

I am also sincerely thankful to Dr Januz Piechna and Dr Witold Selerowicz from Warsaw University of Technology, Poland. Dr Piechna's guidance in the area of CFD modeling was invaluable. My experimental work would not have been complete without the kind support of Dr Selerowicz.

I would also like to thank Dr D. Aslam and his students for their kind help and support in providing us with Si wafers for performing microfluidic experiments.

This work would not have been complete without the keen insight and conversation from my good friend and mentor Ludek Pohorelsky. I would sincerely like to thank him for the knowledge he shared with me, his patience and his never ending enthusiasm and motivation.

I would also like thank my friends and colleagues, especially Marco Vagani, Pranav Sane, Suyash Sidhaye, Gaurav Dabholkar, Amol Patki, Hela Jaziri and Pradeep Kumar and few more for their patience & understanding and also for being there when things did not go as planned.

Last but not the least I would like to thank my parents and my dear sister, for their brilliant support and affection without which I would never be able to make it so far.

TABLE OF CONTENTS

LIST OF TABLES

LIST OF FIGURES

(Images in this thesis are presented in color)

KEY TO SYMBOLS

a	speed of sound (m/s)
A	cross-sectional area (m^2)
Cp	specific heat (J/kg·K)
D	diameter (m)
D_H	hydraulic diameter (m)
e	internal energy (J)
f	friction factor
γ	specific heat ratio
Δp	pressure drop (Pa)
η_P	polytropic efficiency (%)
η	isentropic efficiency (%)
L	channel length (m)
L^*	distance to sonic conditions (m)
k	entrance loss coefficient
M	Mach number
μ	kinematic viscosity (St)
Π	pressure ratio
p	pressure (Pa)
PR_W	wave rotor compression ratio
$\dot{q}$	heat flux (W/m^2)
R	specific gas constant (J/kg·K)
ρ	density (kg/m^3)
Re	Reynolds number
t	time (s)
T	temperature (K)
u	flow velocity (m/s)
u_p	induced flow velocity behind shock wave (m/s)

w shock wave velocity (m/s)

x coordinate along the channel

CHAPTER 1: BACKGROUND AND INTRODUCTION

Every research work has its roots in historical work and past research. This chapter provides a historical perspective and also brief introductions of the state of research in the related works. The idea and motivation behind this effort has been described.

1. 1 Background

The past century has seen a considerable research interest and focus to develop different ways of using heat energy from fuel to generate torque and produce power. Minds across the century have come up with novel ways of converting fuel energy for the purpose of generating torque or propulsion, examples of which are everywhere around us. It began during the Industrial revolution during which in everyday language an 'engine' was any sort of mechanical device that converted some form of energy into mechanical or motion force. The term "gin" as in cotton gin is recognized as originating from the Old French word *'engin'* as a short form of its usage. Beginning from Sadi Carnot's fundamental theory of two stroke reciprocating engine, automotive production has used a variety of energy conversion systems which include electric, steam, solar, turbine, rotary, and piston-type internal combustion engines.

For just over a decade now, the energy community is geared towards designing and now fabricating devices at the meso, micro and even the nano scale. Gas Turbine laboratory at M.I.T, [1, 2] has been a leader in miniaturization of rotational turbomachinery.

(a) Microturbine, (b) Compressor, (c) Combustor & Turbine

Fig 56 From the MIT micro gas turbine project, [3]

Smaller and more functional, power generating devices have been designed and tested but none has been commercialized yet. With the MEMS reactive ion etching technique already developed, batch production and commercialization of such small scale devices with precise geometry is very viable and also a motivating factor to design and study micro scale propulsion, combustors, turbines and other pressure wave exchange devices. This class of research has be named as *Power MEMS* characterized by thermal, electrical, and mechanical power densities equivalent to those in the best large-sized machines produced today, thus producing powers of 10 to 100 watts in sub-centimeter-sized packages. Based on classical thermodynamic cycles (Brayton, Rankine, etc.), such devices would have significantly different behavior than, but equivalent performance to, their more familiar full-sized embodiments. They could see widespread application as mobile power sources, propulsion engines, and coolers. However, the realization of power MEMS presents new challenges both to micromachining and to the traditional mechanical and electrical engineering disciplines of fluid dynamics, structural mechanics, bearings and rotor dynamics, combustion, and electric machinery design, [4] .

The use of unsteady flow devices gives us an interesting alternative to such issues with Power MEMS devices and may provide a way around it.

1.2 Unsteady flow devices

Unsteady flow devices like shock tubes, wave rotors, pulse detonation engines have been around for some time. By exploiting the unsteady flow and pressure exchanges, we can expect a significant increase in engine performance. Also, a less complex, more durable and robust design becomes possible as the use of lot of conventional mechanical components like impellers, and compression pistons is eliminated.

The Wave Rotors also known as Pressure Wave Machines or Pressure Exchangers are unsteady-flow devices that can transfer energy directly between two fluids, by means of pressure waves (shock waves). In a wave rotor, two fluids with different pressures are brought into direct contact. Then pressure exchange occurs faster than mixing. The wave rotor can have a higher isentropic efficiency than steady-flow devices, like compressors or diffusers, but may be more challenging to control. In the past, because of the unsteady nature of the flow inside the wave rotor, process simulation was very inaccurate, time consuming and labor intensive. Recently, because of the increase in calculation power of the computers and more accurate commercially available software packages, significant progress was made in understanding the complex wave phenomena.

Among the most know applications of the unsteady flow characteristics, the Comprex® Pressure Wave Supercharger developed in Switzerland for boosting the pressure in internal combustion engines has found its way into production. The main shortcoming of steady flow devices, like turbochargers, is the lack of boost capability at low engine speed. Devices based on the unsteady flow principle like Comprex, however typically produces higher boost over the entire speed range. The difference is most conspicuous at low engine speed and becomes quite apparent during transient operation.

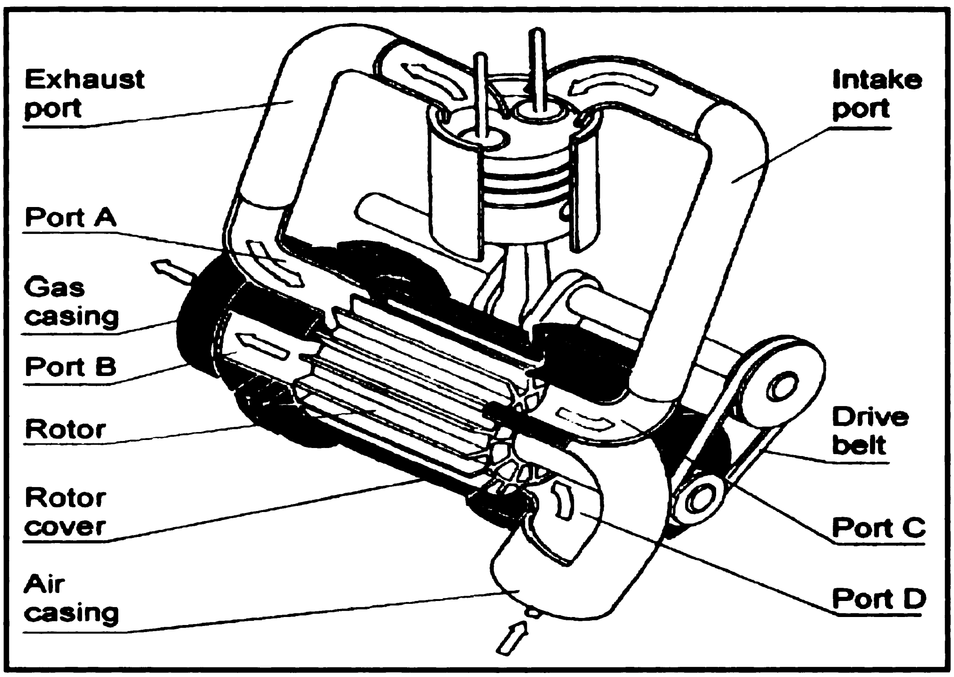

Fig 57 Scheme of a commercial version of wave supercharger – known as Comprex

Early experiments with the PE were made at the beginning of the 20th century by Knauff (1906), Burghard (1913) and Lebre (1928), but the first real application of a PWM was made by Claude Seippel (1940) of Brown Boveri Company (later Asea Brown Boveri), who used it as a high pressure stage for a gas turbine locomotive engine. The best known industrial application of the wave rotor is the

Pressure Wave Supercharger (PWS), which is an alternative pressure-boosting device to the more famous Turbocharger (TC), [5].

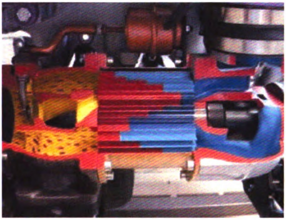


Fig 58 Mazda engine cut-view and the Comprex® rotor

Although extensive tests were made by the BBC from the late 40's until the 80's in order to develop the PWS, the real breakthrough came in 1986 when the Mazda Company introduced its Mazda 626 Cappela model, which had a 2 liter Diesel engine equipped with a Comprex® wave rotor. Mazda produced 150 000 Comprex® Diesel cars, this being the major industrial application for a wave rotor. Other car manufacturer like Opel, Mercedes, Peugeot and even Ferrari used the Comprex® with promising results. To date, the Comprex® is the only commercially available wave rotor, and Swissauto Wenko AG of Switzerland is the only company who produces a modern version of the Comprex®, called the Hyprex®. This type of wave rotor is designed for small gasoline engines applications, [6].

Extensive studies have been done in the past to compare the shock wave compression efficiency and its comparison with diffuser and compressor efficiencies.

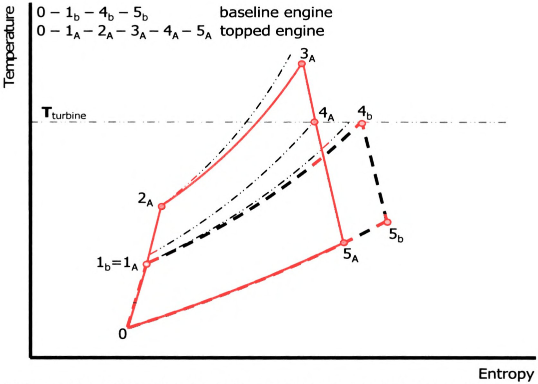

Fig 59 Temperature Entropy diagram for ultra-micro gas turbines, with and without wave rotor, [6]

Figure 59 shows the shows variations of these parameters as functions of the pressure gain p2 /p1 obtained by a shock wave in a frictionless channel and shows it obvious advantage. Besides this, there are several important advantages of wave rotor machines. Their rotational speed is low compared with turbomachines, which results in low material stresses. But they can respond on the timescale of pressure waves, with no rotor inertial lag. From a mechanical point of view, their geometries can be simpler than those of turbomachines. Therefore, they can be manufactured relatively inexpensively. Also, the rotor channels are less prone to erosion damage than the blades of turbomachines. This is mainly due to the lower velocity of the working fluid in the channels, which is about one-third of what is typical within turbomachines [7]. Another important advantage of wave rotors is their self-cooling capabilities. They are naturally cooled by the fresh cold fluid ingested by the rotor. Therefore, applied to a heat engine, the rotor channels pass through both cool air and hot gas flow in the cycle at least once per rotor revolution. As a result, the rotor material temperature is always maintained between the temperature of the cool air which is being compressed, and the hot gas which is being expanded.

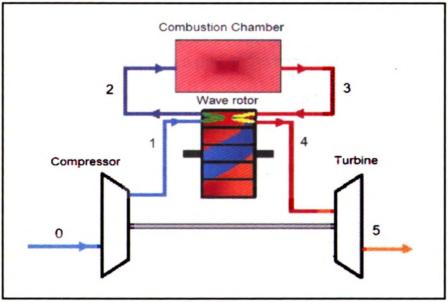

Fig 60 Schematic showing a gas turbine topped by a wave rotor , [6]

Despite very attractive features, several challenges have impeded the vast appearance of commercial wave rotors in some applications though numerous research efforts have been carried out during the past century. Besides unusual flow complexity and anticipated off-design problems and uncertainties about the selection of the best wave rotor configuration for a particular application, the obstacles have been mainly of a mechanical nature, like sealing and thermal expansion issues, as mentioned throughout this study. However, due to the recent energy crises, technology improvement, and economic reasons, new ideas for wave rotor technology have been simulated [6].

1. 3 Microscale power devices

As an improvement to the wave rotor technology, unconventional designs have been proposed and presented. This includes the design and simulations of an Ultra Micro Wave Rotor (UμWR) carried out at the Turbomachinery Laboratory, Michigan State University, [8]. It is a part of the most investigated power sources in the past decade. The class of gas turbines with structures of micrometer size that have been referred to as Ultra-Micro Gas Turbine (UμGT) to distinguish them from small industry gas turbines of 1-250 kW that are often referred to as microturbines, [9].

Due to their high power density, ultra-micro gas turbines (UμGT) are appropriate solutions for powering small unmanned air-vehicles (UAV) and electronic equipment associated with them, such as sensors, probes or cameras. A typical size of a microfabricated (on-the-chip) UμGT is 10mm×10mm×3mm with a power output between 1 and 100 W. Also these microfabricated gas turbines are suitable for high-density, distributed power generation onboard larger aircrafts. Applied in batches they yield high redundancy and reduce the vulnerability of the system. The theoretic power density of turbomachinery increases while their size decreases, the reason is the so called cube square law: The output power is proportional to the mass flow rate of the working fluid that scales with the through-flow area, which is proportional to the square of the characteristic length.

The mass or volume of the engine is proportional to the cube of the characteristic length. Hence Power/Volume is proportional to the inverse of the characteristic length, [10]. One such idea is presented below , Fig 6 which shows a conceptual design of a Ultra Micro Gas Turbine topped with an Ultra Micro Wave Rotor.

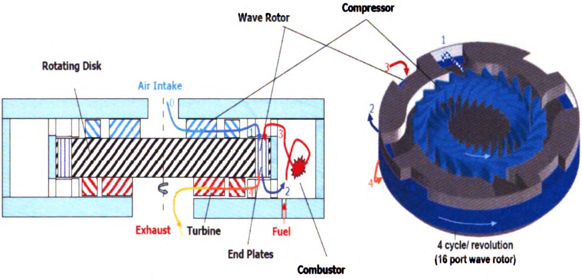

Fig 61 Conceptual design of UμGT – "Classic" design, [8]

For most thermodynamic applications, so far most widely axial-flow wave rotors have been used and investigated. Pure scavenging is a challenging task in the axial-flow configurations. The radial-flow wave (wave disc) concept employs the flow in radial and circumferential directions. This can substantially improve the scavenging process by using centrifugal forces. Figure 7 shows schematically a simple radial-flow wave rotor with straight channels and a rectangular cross-sectional area.

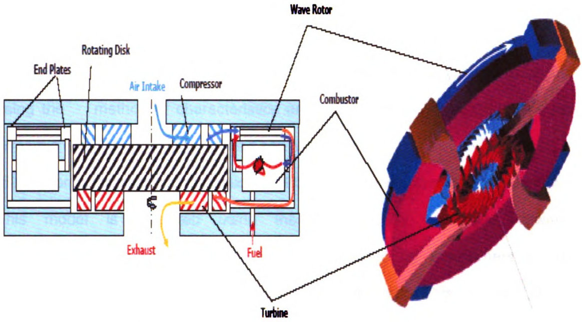

Fig 62 Conceptual design of UμGT – "Radial" design. [8]

1.4 Wave Disc Engine

The concept provided in this work uses a hybrid approach by combining the pressure wave exchange principle for transfer of energy and utilizing the internal combustion (constant volume) principle, at a micro scale to generate the energy. By using appropriate geometry of the channels, channels port timings can be used to generate the change of angular momentum. Not much literature is available at this moment which talks about an independent power generating wave disc concept. Piechna, et. al have proposed a similar design with a separate combustion chamber, [11] .

1.5 Work presented

This work has covered more than one facets of a preliminary design for wave disc engine. Numerical and experimental work leading to understanding of important concepts in design of this micro scale device has been presented. The work includes:

(A) Numerical model of the micro scale internal combustion wave disc engine using the method of characteristics and normal shock wave relations. Gas Dynamic wave diagram is presented and explained.

(B) A Computational fluid dynamics (CFD) model of the wave rotor is presented. This model is prepared using the commercially available software, FLUENT®6.2.Port geometries have been optimized by researchers at the Turbomachinery Laboratory at Michigan State University. This is a part of the wave rotor test rig being built and tested here at the Turbomachinery Laboratory, MSU.

(C) Micro fluidic experiments to compute friction factor in four different lengths micro channels inside a Silicon wafer, were performed at University of Technology, Warsaw. Friction factors, as one of the fluid flow characteristic, was studied, calculated and compared with the theoretical values.

CHAPTER 2: WAVE DISC ENGINE THEORY

This chapter explains the gas dynamic theory behind the wave disc engine and the working principle. Basic wave theory is also explained, along with the wave and state diagram of the wave disc engine.

2. 1 Wave Theory

The understanding of wave theory gas dynamics is crucial to developing the wave disc engine. It is very convenient and easy to explain this concept using a single stationary channel, very similar to a shock tube. The wave diagram, as shown in figure 8, is a way to represent gas motion on a time versus space plot. When the wall or a diaphragm is broken between the two regions at different pressures is broken, typically two types of 'waves' are generated at the point on rupture. A shock wave travels towards right into the low pressure region or the driven section. The wave which travels towards the left is the expansion wave and it's also referred to as the driver section. The shock wave increases the pressure and temperature of the driven section rapidly and induces a mass motion behind itself. The interface between the driver and driven gases, called the contact surface, moves with an induced velocity in the same direction as the incident shock. The expansion wave decreases the pressure and temperature of the driver section smoothly. Therefore, across the contact surface the pressure and velocity are preserved while the temperature and entropy change discontinuously.

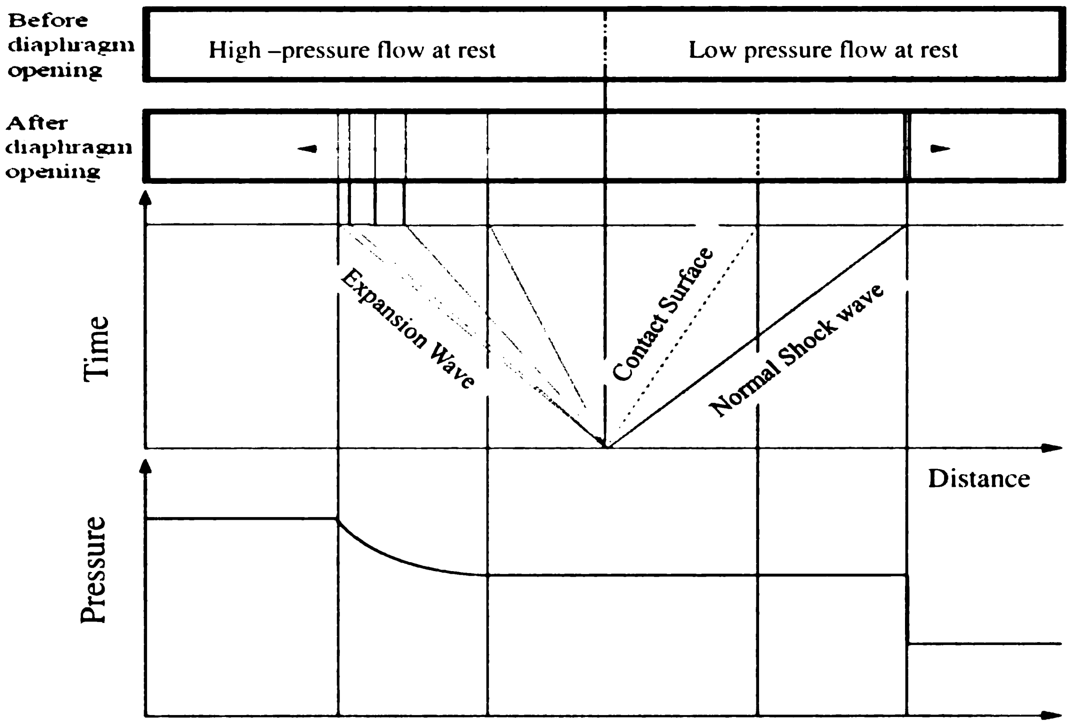

Fig 63 Flow behavior inside a tube when the diaphragm is suddenly ruptured, [12]

2.1.1 Shock wave generation

In unsteady flow devices shock waves are typically generated by either sudden opening of the port or like in wave disc engine design, sudden closing of the port. This is explained with the figure 9. When the fluid is suddenly brought to rest by closing the channel, it generates a shock wave in the direction opposite to the incoming fluid flow velocity. As this shock wave travels towards the left, it brings the fluid at rest and thus raising the pressure of the fluid.

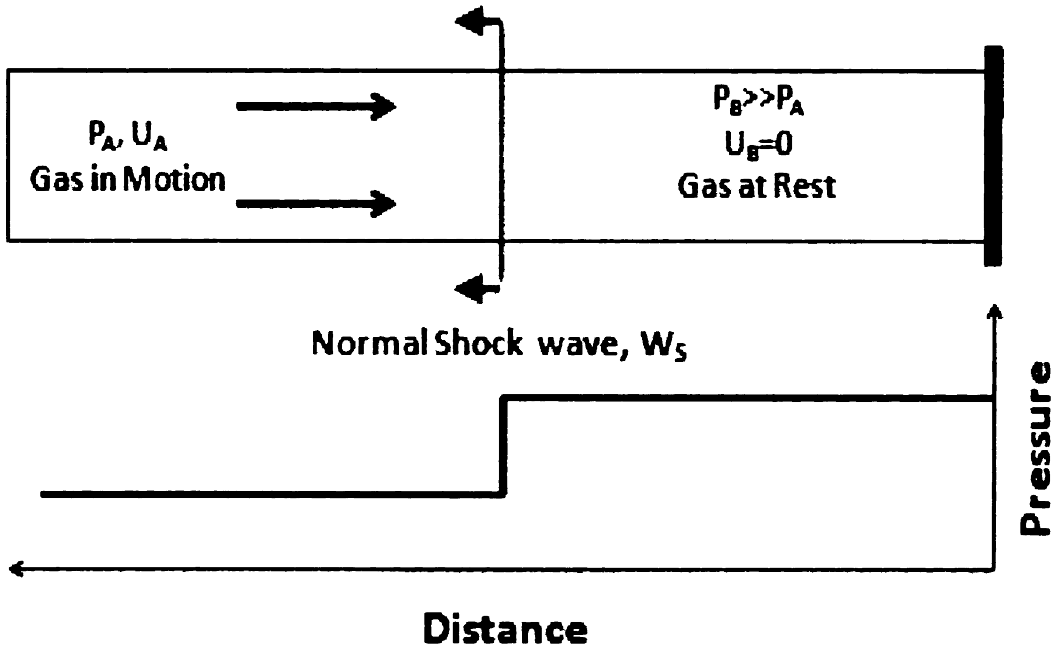

Fig 64 Shock wave generated as the channel is suddenly closed on the right

2.1.2 Expansion wave generation

When a gas at high pressure is suddenly exposed to lower pressure, it expands. When the end of the tube is rapidly opened, it results in the formation of an expansion fan which propagates inside the tube inducing a gas flow out of the tube. Such a scavenging flow process imitates the expansion process of the driver section in a shock tube after sudden removal of the diaphragm. Another way of expansion wave generation is by sudden closing of the flow (left port of the shock tube shown in figure 8). Because the velocity of the gas in contact with the closed end must be zero, an expansion wave propagates into the moving gas, bringing it to rest. Note the pressure drop is not as sudden as in a shock wave, as show in figure 10.

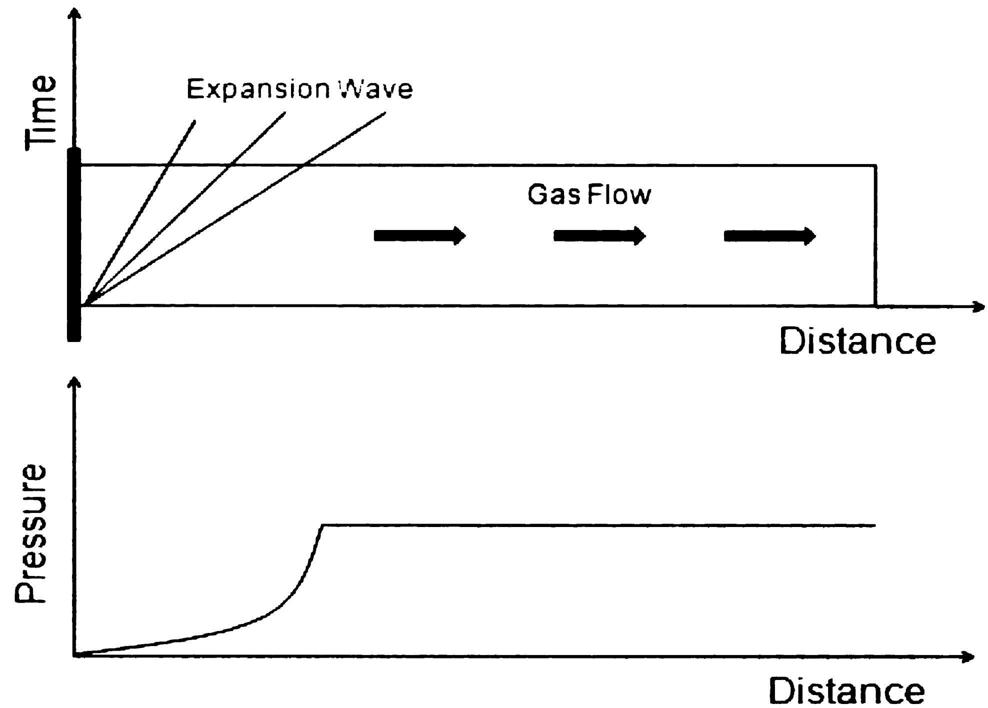

Fig 65 Expansion wave generated as the channel is suddenly closed on the left

The above shown schematics show that sudden closing of a channel generates shock and expansion waves inside a channel or a tube depending on the port position and fluid flow direction.

For this work, the flow is assumed to be adiabatic, frictionless, and reversible. For such isentropic behavior *method of characteristics* is used to compute the pressures and flow properties. This is isentropic compression and expansion.
The final compression is before the combustion is assumed to be taking place with a non-isentropic, yet adiabatic pressure wave, i.e. a shock wave. In subsequent chapters, the logic behind this assumption is explained along with the analytical model.

2. 2 Principle of Operation

The cycle of operation is explained with a schematic, Fig 11 and wave diagrams in absolute, Fig 12 and relative frames, Fig 13, are explained.

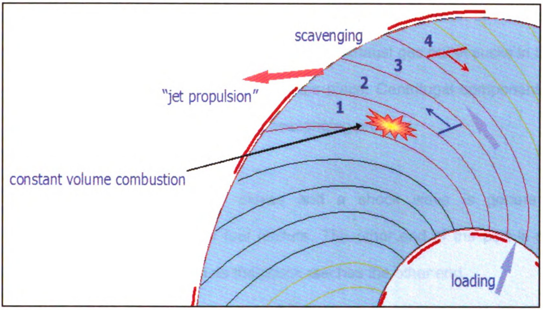

Fig 66 Schematic showing the wave disc engine cycle

1. Constant volume combustion takes place of the compressed air fuel mixture. Channel closed at both ends. Combustion (Deflagration) taking place near the middle. High pressure exhaust gases starts to accumulate at other end. Port timing has to be such as to not let a reverse shock wave develop.

2. Expansion of these high pressure and temperature begins as outer end of the channel opens to ambient conditions. Torque generation is expected in this process. Channel geometry can be so designed as to generate

partial propulsion from the exhaust gases. The tangential component (using the Turbomachinery principle or Jet propulsion) will be added to the net torque. This sudden expansion begins partial scavenging.

3. The inlet port, at ambient conditions, opens up and ingestion of fresh fuel air mixture begins. Expansion wave due to exhaust gas outlet sucks in this mixture and complete scavenging takes place. Centrifugal component of the disc also partially helps in the scavenging process.

4. The outlet port suddenly closes and a shock wave is generated compressing the fresh air fuel mixture. The other end of the port is still open and closes as soon as the shock reaches the other end.

The next figure indicates the wave pattern in a relative frame of reference. Wave propagation is plotted over a distance versus time plot. It also indicates the flow velocity. It must be understood that the flow velocities depicted in this diagram is the net flow velocity and not the instantaneous flow velocity. The width of the velocity vectors gives a good understanding about the flow velocity magnitude as well. The red arrows represent the compression wave and the blue arrows represent the expansion wave.

The red channel indicates the channel just after combustion. It is the region of high pressure and temperature. As the channel moves, it first opens to the exhaust port, which is assumed to be at ambient conditions. Due to this sudden opening to a low pressure region, an expansion wave starts at the beginning of the exhaust port and travels towards the inlet port, between Zone II & III. The flow velocity is in the direction opposite to the expansion wave. The burnt exhaust gases rushes out of the channel with this velocity. As the first expansion wave reaches the opposite end, it gets reflected back just before the inlet port opens. The induced flow velocity by this strong expansion wave is very high. This expansion provides the motion to the disc and is the source of torque. This is also the beginning of the scavenging process.

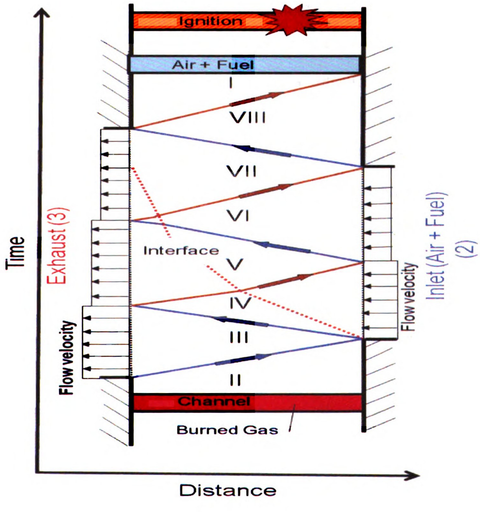

Fig 67 Wave diagram showing the wave propagation on a relative frame of reference

The second expansion wave which is a reflected expansion wave, between Zone III and IV travels, is a weaker expansion wave. The induced flow velocity by this wave is lesser in magnitude and opposite in direction of the previous flow direction. But the net flow velocity is still in the direction towards the exhaust flow. This net induced flow brings in the fresh air fuel mixture into the channel. At this point of time we have an interface between the unburnt charge and the exhaust gases inside the channel. This is depicted with the red dotted line beginning in Zone IV.

The boundary conditions which we have assumed for this model is that at exhaust, the static pressure is slightly above atmospheric conditions and at inlet, the static pressure conditions is slightly below atmospheric. As the second expansion wave reaches the exhaust port boundary, due to a pressure difference between Zone IV & V, a pressure wave (red) originates. This pressure wave and the net fluid velocity it induces is still in the direction of the exhaust port.

As this first pressure wave reaches the inlet port which is less than atmospheric, the third expansion is generated, and it travels towards the exhaust port. During these really fast wave exchanges, scavenging takes place as shown by the charge-exhaust gas interface. The channel is now almost filled with the fresh air fuel mixture.

As the fourth expansion wave reaches the exhaust port end, the net induced velocity is at its minimum. The exhaust port rapidly closes and due to this rapid closure of end of a channel, a shock wave is generated, as depicted in the third red arrow. This shock wave acts as the compression wave Zone VIII - I and increases the pressure and temperature of the charge just before the constant volume combustion takes place which again starts the cycle.

This process is explained using figure 12, which shows the wave propagation. Figure 13 indicates the wave propagation in an absolute frame of reference.

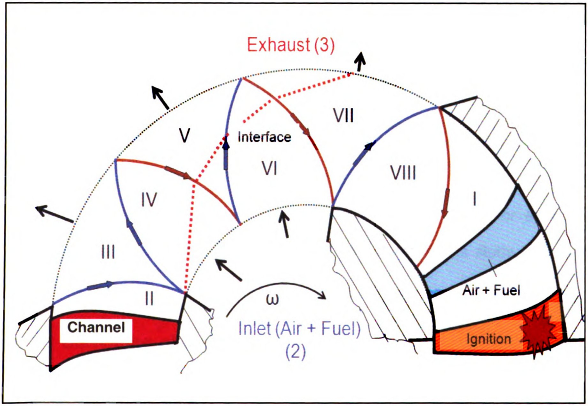

Fig 68 Wave diagram showing the wave propagation on an absolute frame of reference

The expansion of the exhaust gases generates the necessary reaction force to rotate the disc and generate torque. This torque can be transmitted to a center shaft and used as power. This design encapsulates constant volume combustion inside the microchannel. Combustion has been modeled by constant volume heat addition.

Chapter 3 Gas Dynamics of Wave Disc Engine

This chapter discusses the analytical technique which has been used to develop the numerical code for optimizing and calculating the wave disc behavior.

3.1 Method of Characteristics

Due to the assumed isentropic nature of compression and expansion waves, the method of characteristics can be used to find the flow properties across the wave. This method is a very general and powerful technique for analyzing compressible flow. For the specific problem considered in this study, only one-dimensional version of this method is used.

3.1.1 Derivation of the characteristic line

The isentropic relations are:

$$\frac{p}{p_0} = \left[\frac{\rho}{\rho_0}\right]^{\kappa} = \left[\frac{a}{a_0}\right]^{\frac{2\kappa}{\kappa-1}} = \left[\frac{T}{T_0}\right]^{\frac{\kappa}{\kappa-1}} \qquad [1]$$

and the local speed of sound, a is given by

$$a = \sqrt{\kappa R T} \qquad [2]$$

The pressure relations for an expansion and compression wave relations can be formulated using a piston analogy as shown in figure 14. This diagram shows the beginning of expansion wave as the piston head reaches top dead center (TDC).

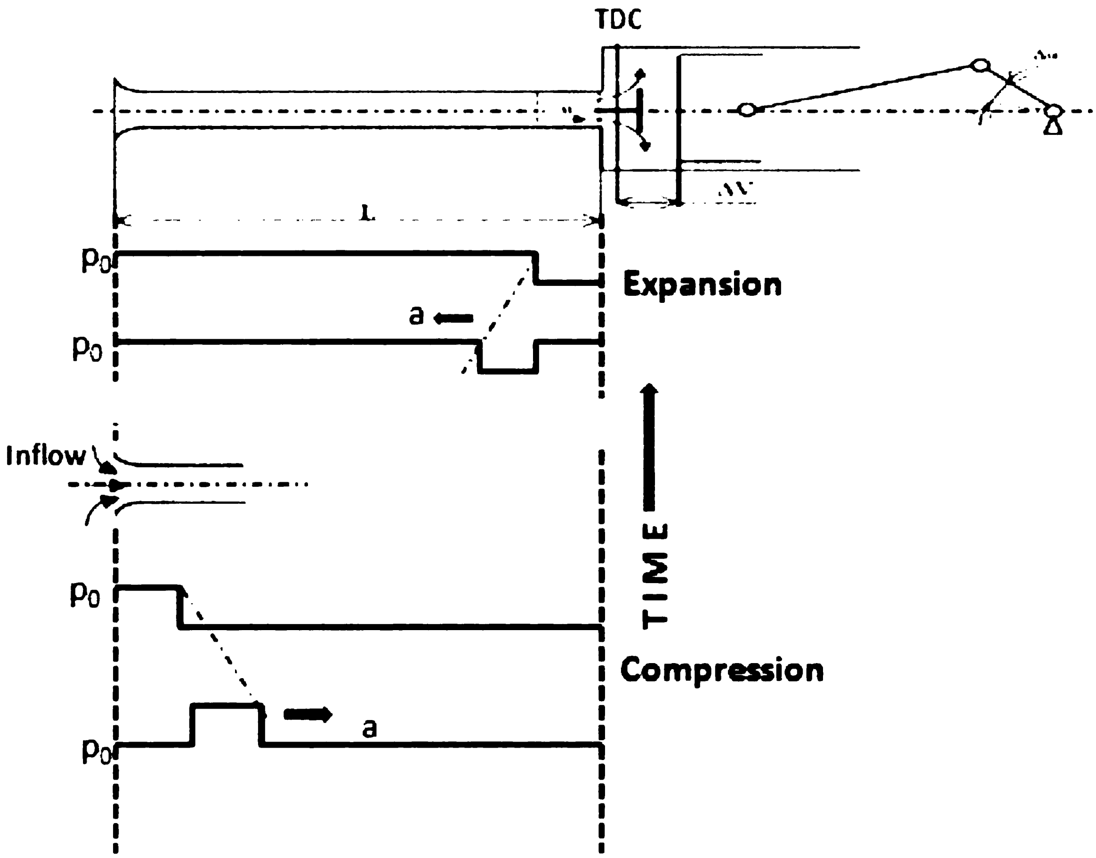

Fig 69 Propagation of the expansion wave and its reflection at the open end

The expansion wave propagates towards left with the local speed of sound given by equation 2. As this expansion wave reaches the left end, there is a sudden inflow. This produces a compression wave which travels in the opposite direction with the local speed of sound.

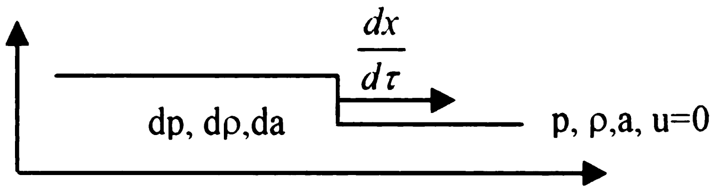

Fig 70 Change of state properties as the wave propagates

This wave disturbance produces a change in properties as shown in figure 15 and induces a flow. We will now develop the relations for the change in properties.

Consider a single element of uniform cross sectional area A. The direction of the induced flow is opposite to the direction of the travelling wave, as this is an expansion wave.

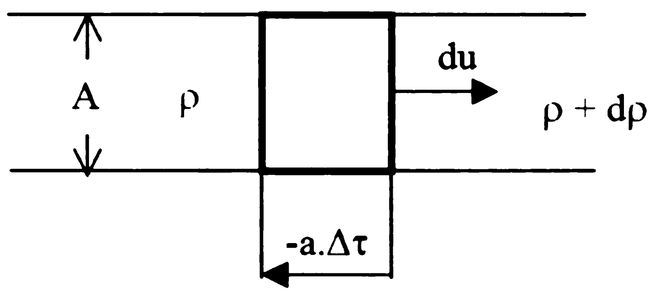

Using the mass balance relationship we get

$$\Delta m = \Delta m_{out} - \Delta m_{in}$$

$$-a.d\rho.\Delta\tau = du.(\rho + d\rho).\Delta\tau - 0$$

$$-a\frac{d\rho}{\rho} = u$$

From the differential form of the isotropic relations we get

$$\frac{d\rho}{\rho}=\frac{2}{\kappa-1}\frac{da}{a}$$

Using these relations we get

$$du=-\frac{2}{\kappa-1}da$$

Integrating this we have the following equation

$$u+\frac{2}{\kappa-1}a=Const.$$

Now dividing this relation throughout by a_0 as this will make the representation and the computation a lot easier.

$$\frac{u}{a_0}+\frac{2}{\kappa-1}\frac{a}{a_0}=\frac{Const.}{a_0} \qquad [3]$$

And using the following substitutions

$$U=\frac{u}{a_0}$$

$$A=\frac{a}{a_0}=P^{\frac{\kappa-1}{2\kappa}}=\left[\frac{p}{p_0}\right]^{\frac{\kappa-1}{2\kappa}}$$

From Equation 3 and these substitutions we get

$$A=-\frac{\kappa-1}{2}U+C \qquad [4]$$

Where

$$C=\frac{Const}{a_0}\frac{\kappa-1}{2}$$

Equation 4 is an equation of a straight line which will represent the state properties change as it moves from one point to other. Also from the substitutions, equation 4 can also be represented as

$$P^{\frac{\kappa-1}{2\kappa}} = -\frac{\kappa-1}{2}U + \frac{Const}{a_0}\frac{\kappa-1}{2} \qquad [5]$$

To find out the constant part we find out the conditions when U=0, also we will make another substitution $P_\lambda = \frac{p_\lambda}{p_0}$

So equation 5 becomes

$$P^{\frac{\kappa-1}{2\kappa}} = \frac{Const}{a_0}\frac{\kappa-1}{2} = P_\lambda^{\frac{\kappa-1}{2\kappa}}$$

$$P^{\frac{\kappa-1}{2\kappa}} = -\frac{\kappa-1}{2}U + P_\lambda^{\frac{\kappa-1}{2\kappa}} \qquad [6]$$

Equation 6 is also an equation of the line of the form $y=mx+c$, where m is the slope of the line. And it can be represented as shown

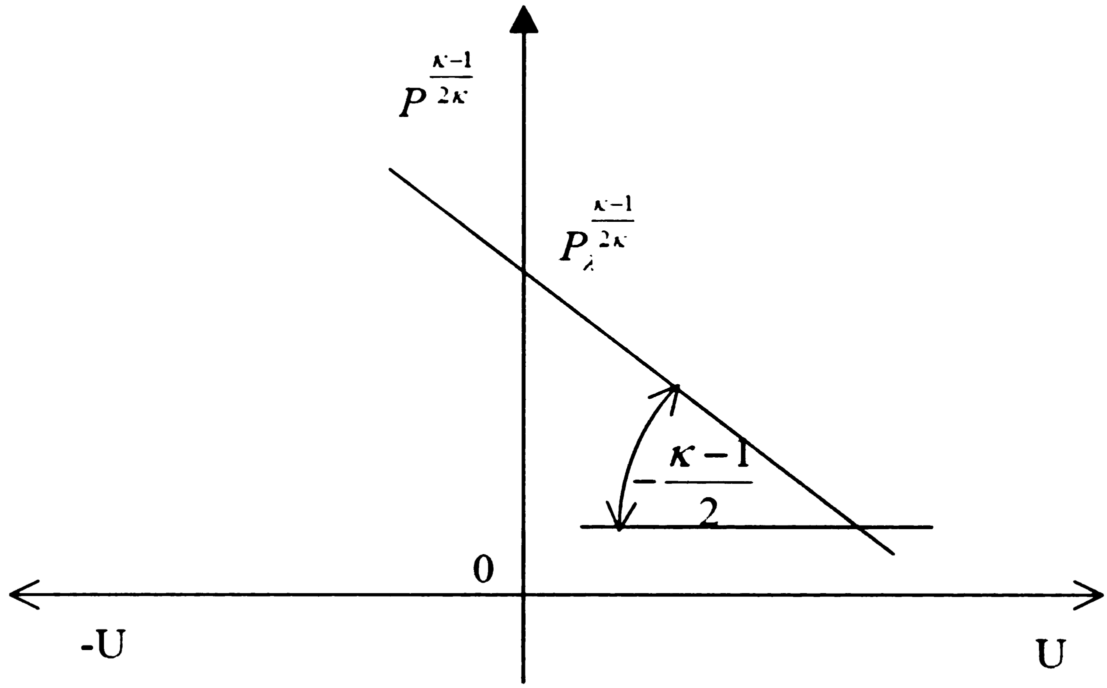

Fig 71 State Diagram depicting the expansion wave

Figure 16 shows the line of equation 6 with the slope. In the similar derivation, the line for compression wave with the induced velocity in the same direction can be depicted with a positive slope. The derivation is similar and can be written as:

$$P^{\frac{\kappa-1}{2\kappa}} = \frac{\kappa-1}{2}U + P_{\lambda}^{\frac{\kappa-1}{2\kappa}} \qquad [7]$$

Note the sign change of the slope. Now we have the basic understanding to develop the characteristic lines on a state diagram.

3.1.2 Generalization of the characteristic lines

We can now generalize the characteristic lines in all four quadrants of the state plane. The following diagram depicts all four quadrants. The initial conditions in the tube are taken to be $p_0=p_\lambda=1$ bar as shown by [0, 1] on the abscissa. This diagram gives us clear information about the direction and properties of the wave propagating in any particular direction.

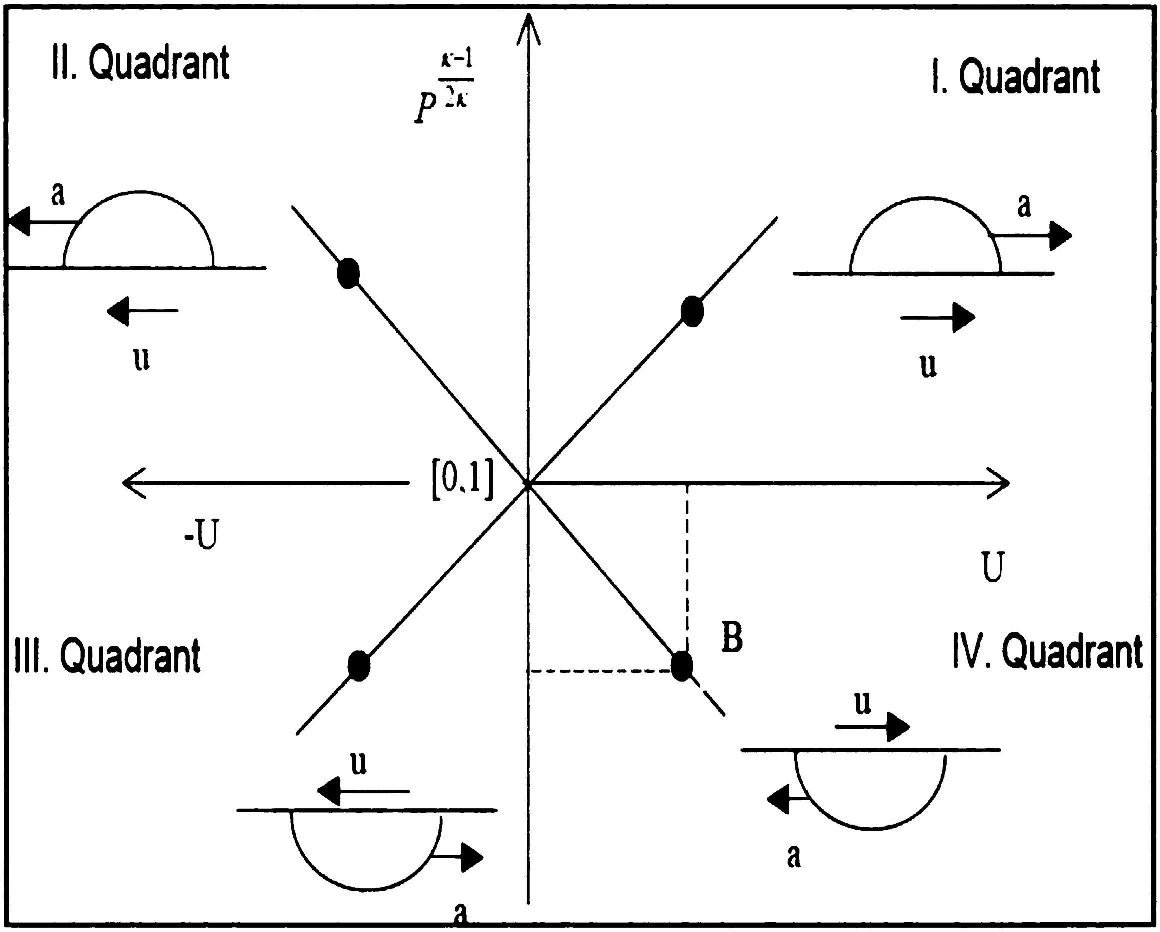

Fig 72 State Diagram depicting compression and expansion waves in all four quadrants

The direction of '*u*' indicates the direction of induced flow and the direction of '*a*' show the direction in which the wave is propagating. The case talked about earlier is shown in quadrant IV, which shows and expansion wave travelling left. The point B will depict the flow velocity and pressure at that instance. The other properties can be computed if we have the knowledge of these state properties. Quadrant I shows a compression wave travelling right and the induced flow in the same direction, right. Quadrant II shows the compression wave and induced flow in the same direction but travelling towards left. Quadrant III shows an expansion wave travelling towards right and induced flow in the opposite direction.

3.2 State Diagram of the wave disc engine

Now we will be representing the wave disc cycle on a state plane and then formulate it in a mathematical form with the technique discussed earlier.

The state diagram of the wave disc engine, figure 18 depicts in a legible form the dependency between normalized pressure $(p/p_0)^{\frac{\kappa-1}{\kappa}}$ and normalized induced flow velocity (u/a_0). Positive flow velocity means flow direction to right [13, 14]. The lines, so called state characteristics, within the axes of normalized flow velocity and normalized pressure show the changes in the state within the disc channels between boundary conditions represented by lines of Air Inlet (AI), and Exhaust Outlet (E0).

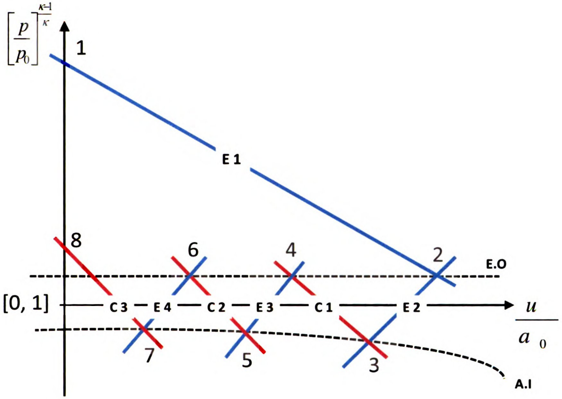

Fig 73 State diagram representing the wave disc engine cycle

Using this diagram it was possible to analyze the interdependency of the velocities and pressures of each of these zones by varying any one of them. The slopes of the state characteristics have been set according to the K and temperature of the fluid that the wave is propagating through. For our calculations we have assumed ideal gas conditions and for channels with both gas & air and with just gas, we have used a correction factor.

The process begins at State 1, which is just after combustion and the fluid is at zero velocity. The expansion wave E 1 travels from left to right with a negative slope and changes the properties from State 1 to State 2. At State 2, it reaches exhaust outlet boundary conditions and the second expansion wave, E 2 originates and travels towards left side. As it reaches the Air Inlet port a compression wave C 1 starts and travels to the EO with a negative slope. Due to the high strength of the first expansion wave the net induced velocity will continue to cause scavenging and help suck in the fresh air fuel mixture charge in. For the ease of simplification we will assume the 'K air' for the fuel air mixture. As C1 reaches EO, the third expansion wave E 3 begins traveling left with a positive slope. These wave exchanges takes place till state 7, where the air inlet port suddenly closes and a strong compression wave travels towards exhaust outlet. This is state 8. This closing is so timed so that the channel is now just filled with fresh air fuel mixture, compressed by C 3 and ready for the constant volume combustion.

3.2.1 Governing Equations

Change of state (see Fig. 18) by this and also by the subsequent waves has been described using method of characteristics as described earlier, by applying the relationship between state quantity (local speed of sound) and the flow velocity in the well known form :

$$da = \pm \frac{\gamma - 1}{2} du \qquad [8]$$

For the change of state by expansion wave propagating between states 1 and 2 and travelling towards the right can be shown by using the normalized state quantities:

$$\frac{a_1}{a_0}-\frac{\gamma-1}{2}\cdot\frac{u_1}{a_0}=\frac{a_2}{a_0}-\frac{\gamma-1}{2}\cdot\frac{u_2}{a_0} \qquad [9]$$

For a wave propagating between State 1 and 2 and travelling towards the left follows:

$$\frac{a_1}{a_0}+\frac{\gamma-1}{2}\cdot\frac{u_1}{a_0}=\frac{a_2}{a_0}+\frac{\gamma-1}{2}\cdot\frac{u_2}{a_0} \qquad [10]$$

As pressure waves work on the same theory as expansion waves, we can use equation [8] – [10] to describe the pressure wave propagation as well.

Owing to the low pressure ratio between the states, both pressure waves and expansion waves are weak and hence the waves were computed using method of characteristics. Equations [8] – [10] are written for waves propagating only in air. Nonetheless, in the wave disc engine the pressure or expansion waves propagate in mediums of different temperature and composition (hot exhaust gas and cold fresh air).

According to [8] and [10] the state characteristics – (see equation [8]) - for wave propagating in exhaust gas yields to:

$$d\left(\left(\frac{p}{p_0}\right)^{\frac{\gamma_{air}-1}{2\gamma_{air}}}\right)=\pm\frac{\gamma_{air}-1}{2}\cdot\frac{a_{0air}}{a_{0gas}}\cdot\frac{\gamma_{gas}}{\gamma_{air}}d\left(\frac{u}{a_{0air}}\right) \qquad [11]$$

From Eq. [11] follows that the magnitude of the induced flow velocity differs for gas and air. In the introduced algebraic code, if the waves propagate both in gas and in air the average of the induced flow velocities has been used for estimation of the flow velocity in particular state.

3.2.2 Calculation of the Gas Air Interface

The code calculates the position of the gas-air interface at all zones which helps analyze the scavenging ability of the design geometry and the operating conditions. For example, to calculate the position of the interface in the HP region, we know that the flow velocity for both mediums (air and gas) are the same but the local speed of sound varies with temperature and thus influences the wave propagation speed in different media.

The analytical code is based on these equations and the results will be presented in the results section.

3.2.3 Boundary conditions

For the inlet and outlet of channels a quasi steady consideration has been applied, i.e. it was assumed that a fast running wave will create a steady state at the inlet and outlet ports, [13] .In the state diagram, figure 18, it is represented as an intersection point of state characteristics (non-steady flow or the expansion and compression lines) and equation of boundary condition (steady state flow).

It was assumed that at AI, the flow comes in from a reservoir or zero velocity, and using the energy balance between the zero velocity reservoir conditions and flow speed conditions inside the channels, the following inlet boundary condition was used.

$$\left(\frac{a_1}{a_0}\right)^2 = \left(\frac{a_2}{a_0}\right)^2 + \frac{\gamma-1}{2}\cdot\left(\frac{u_2}{a_0}\right)^2 \qquad [11]\,a$$

which is an equation of an ellipse and can be seen as the AI condition in the state diagram, figure 18. For the outflow boundary condition from the channel, it is assumed that the wave reflects from the constant pressure at the end opening, i.e. the fluids assume the constant static pressure in the outflow ports.

3.3 External combustion wave disc engine; an overview

The engine has only one rotating part, a compression–decompression disk and a combustion chamber. In figure 19 a double port set with two parallel operating combustion chambers with one step compression is shown. Arrows in the figure explain the used flow field scheme. According to Epstein [1] and Frechette [10] the motor–generator can be integrated within the engine.

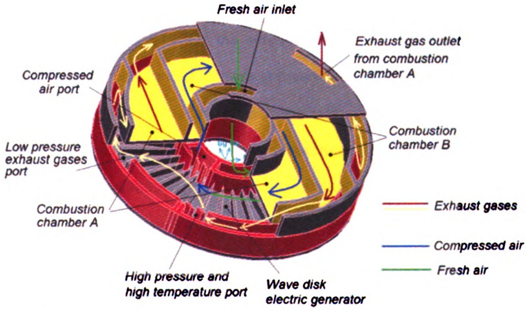

Fig 74 Possible construction of the single-stage compression wave engine in reverse-flow configuration, [11]

The working principle of the single stage compression wave engine is neatly described using the wave diagram in Figure 20.

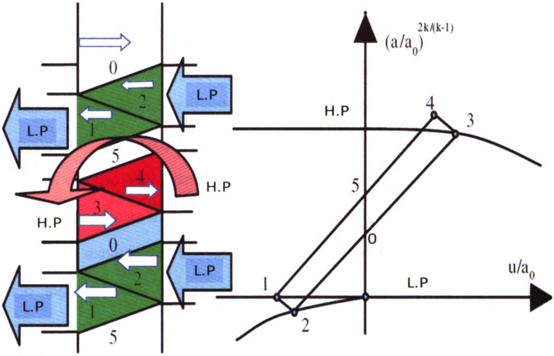

Fig 75 Single-stage compression wave engine scheme in reverse flow configuration, [11]

The flow scheme of an external combustion wave engine is based on the wave diagram shown in figure 19. On the left-hand side of the drawing, a schematic wave diagram with positions of all ports is presented with the corresponding state plane on the right-hand side. Flow parameters in areas on the wave diagram, separated by waves, compression and expansion, are constant and are described by the corresponding points on the state plane.

Numbers in wave diagram areas have equivalents on the state plane. Expanded exhaust gases are rejected to the atmosphere (area 1) generating an expansion wave inducing inflow of the fresh air (area 2). Fresh air is compressed (area 3) by the high pressure hot gas from the combustion chamber. Compressed air (area 4) is delivered to the combustion chamber. After heating in the combustion chamber the hot mixture of air and exhaust gases is used for fresh air compression and after expansion is rejected to the atmosphere.

The single-step compression reverse-flow wave engine configuration shown in figures 19 and 21 was the first one considered. In figure 21 the exploded view of the main wave-engine components is shown. Rotor diameter is 30 mm, [11].

The engine case can be prepared as a three part set. The most complicated part contains the basic plate with all port arrangements. The second part forms the combustion chambers and outflow mufflers. The third part is only the cover with air inlets and exhaust gas outlets. The wave disk can be formed from two parts etched together. The engine has only one rotating part, a compression–decompression disk. The electric motor–generator can be imprinted in the case part containing ports and in one of parts forming a wave disk as is shown in figure 21.

Fig 76 Exploded view of the wave-engine construction, [11]

Other wave-engine constructions have also been considered. A wave engine can also be built in the through- flow configuration. Higher engine efficiency can be realized in the two step compression configuration. Double-stage compression devices were considered and a detailed design is presented in figure 22.

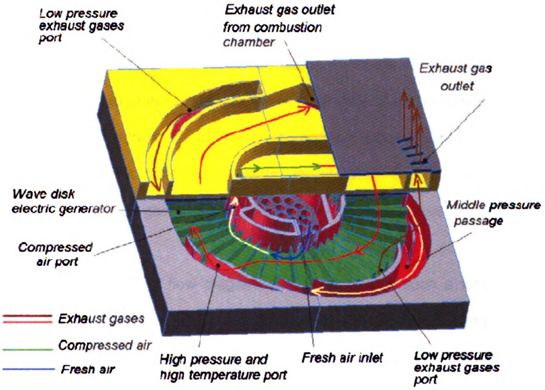

Fig 77 Details of the two-step compression wave-engine construction, [11]

In the proposed solution on the outer side of the wave disk the high pressure gas port (port B), two middle pressure gas ports (inlet (port A) and outlet (port C) connected by a passage, and low pressure gas outflow port (port D) are located. The high pressure air port (port E) and low pressure fresh air port (port F) are located on the inner side of the wave disk. In such a configuration the fresh air enters the cell with pressure and velocity described by the position of point 9 on the state diagram, then air is compressed to state 1, on the state plane, by the middle pressure gas entering the cell from the middle pressure passage with parameters described by point 6, and air is finally compressed to state 4 by the high pressure gas. Air compressed twice to the high pressure is delivered to the combustion chamber.

After mixing with the fuel it forms the mixture which is burned inside the combustion chamber. Hot, high pressure gases leave the combustion chamber and enter the cell at state 3 realizing the second step of air compression. Then exhaust gases leave the cell and through the medium pressure passage (state 6) enter the wave disk cells again (state 1), realizing the first stage of air compression. Exhaust gases finally, after decompression, leave the cell to the exhaust port (state 8).

The port's geometry and flow diagram are developed in such a way that hot gases are concentrated near the outer part of the wave disk and cold air concentrates near the inner disk part. On the one hand such a configuration generates non uniform temperature distribution and thermal stresses in the disk, but on the other hand it reduces the heat exchange between disk walls, cold air and hot gas. Generally this flow arrangement can be classified as the reversed flow configuration, [11, 14].

The flow scheme was matched to the radial wave rotor geometry used in the proposed solution. It was assumed that centrifugal forces can improve the flow during the scavenging and slightly disturb the compression process. There is enough energy during the compression process to overcome the negative influence of centrifugal forces. The energy available during the end of the scavenging process is not sufficient to completely remove exhaust gases from cells. In that phase of the flow, centrifugal forces act in a way that improves the scavenging process in the proposed configuration.

For the combustion modeling compressed air leaving the wave disk through port E (figure 19), located on the inner disk side, is delivered to the combustion chamber, then heated and returned to the cells of the wave disk through port B (figure 13), on the outer side of the disk. The pressure and temperature in the combustion chamber can be calculated from the energy and continuity equation and equation of state:

$$\frac{dp}{dt} = \frac{\kappa - 1}{V_{comb}} \begin{pmatrix} \rho_{air} u_{air} F_{air} \left(\frac{\kappa R T_{air}}{\kappa - 1} + \frac{u_{air}^2}{2} + \frac{V_{out}^2}{2} \right) \\ - \rho_{gas} u_{gas} F_{gas} \left(\frac{\kappa R T_{gas}}{\kappa - 1} + \frac{u_{gas}^2}{2} \right) + Q_{comb} \end{pmatrix} \quad [12]$$

$$\frac{dm_{V_{comb}}}{dt} = \rho_{air} u_{air} F_{air} - \rho_{gas} u_{gas} F_{gas} \quad [13]$$

$$T = \frac{p V_{comb}}{R m_{V_{comb}}} \quad [14]$$

The flow scheme in this kind of micro-engine was designed to generate a net power. In the proposed engine version, [11] only straight cells are used. All ports in which the flow is in the disk direction are expected to be equipped with vanes directing the port flow almost tangentially to the disk.

From the equations of continuity and spin conservation the torque can be calculated. Only in a relatively narrow range of engine port geometry and rotational speed may positive torque and power be generated.

CHAPTER 4 COMBUSTION AT MICRO SCALE

The internal combustion taking place inside the channel is occurring at a micro scale. This chapter will deal with the issues and approaches surrounding this complex phenomenon. The concept behind this new field of high-specific-energy micro-electro-mechanical power systems is to utilize the high specific energy of liquid hydrocarbon fuels in combustion driven micro-devices to generate power.

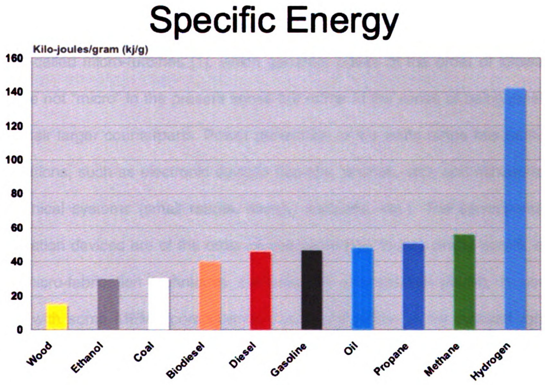

Fig 78 Specific energy for different energy producing devices, [15]

Liquid hydrocarbon fuels have extremely high specific energy, (typically 45 MJ/kg) as compared to 1.2 MJ/kg for a lithium or 0.6 MJ/kg for an alkaline battery. These miniature combustion devices with just about 3% efficiency would compete with top batteries simply from the fact that the fuel is easily replaceable. Although higher efficiencies are needed for combustion systems to displace batteries, the high efficiencies obtained in large-scale power systems encourage the development of miniaturized power generation devices using combustion, with the expectation that devices with competitive efficiencies can be developed. Another interesting and attractive aspect of miniaturization is the batch fabrication capabilities availability of MEMS using rapid prototyping techniques with their mass production and low cost characteristics, [15].

The power-generation devices addressed in this chapter are those that aim to generate power in the range of a few watts to milliwatts. This is in contrast with the so-called micro-turbines [1], which generate power of the order of kilowatts and are not “micro” in the present sense but rather in the sense of being smaller than their larger counterparts. Power generation in the watts range has multiple applications, such as electronic devices (laptops, phones, etc), and miniaturized mechanical systems (small robots, rovers, airplanes, etc.). The corresponding combustion devices are of the order of one centimeter in size (meso-scale), and their micro-fabrication techniques are relatively conventional (EDM), in some cases with some MEMS components. Power generation in the milliwatt range (micro-scale) has its application primarily in micro-electronic components (sensors, transmitters, etc), with the ultimate goal of incorporating the power-generation device into the micro-electronic component. These power generation devices are constructed using primarily MEMS. The ultimate goal is to have "power generation in a chip". The system would then incorporate in the same unit the power device, the microprocessor to control the overall system, and some sort of sensor/emitter or actuator, [15].

Small-scale combustion has other useful applications than power generation and heat production for use in power cycles. Positioning of localized heat is an important example of its potential applications. Another interesting example is the use of arrays of meso-scale burners to produce distributed combustion in large scale gas turbine combustors, which has the potential for inter-turbine reheat, and for premix or highly vitiated combustion, to reduce NOx [16].

We will now discuss some thermo-chemical and technological issues for power generation devices.

4.1 Thermo-physical Aspects of Micro combustion

The characteristic length gives a measure of the average distance that the products of the burnt fuel must travel to escape. In the present available designs, this length is sufficiently larger than the than the molecular mean-free path of the air and other gases flowing through the systems that the physical-chemical behavior of the fluids is fundamentally the same as their macro-scale counterparts. For example, the Knudsen number for air flowing through a 0.1 mm wide channel is of the order of 10^{-3}, which is much smaller than that for free-molecule flow ($Kn > 1$), [15]. So we are led to believe that standard no-slip condition and the continuum hypotheses will still apply.

However, the small size of these devices causes some scaling issues which causes some interesting changes to particular characteristics of fluid mechanics and heat transfer.

These can be understood by normalizing the conservation equations of momentum, energy and species in terms of the characteristic length and parameters of the device and analyzing them as the length scale is reduced, [15].

$$\frac{l_c}{t_c u_c}\frac{\partial \overline{u}}{\partial \overline{t}} + \overline{u}\frac{\partial \overline{u}}{\partial \overline{x}} = -\frac{p_c}{\rho_c u_c^2}\frac{1}{\overline{\rho}}\frac{\partial \overline{p}}{\partial \overline{x}} + \frac{1}{\mathrm{Re}}\overline{\nu}\frac{\partial^2 \overline{u}}{\partial \overline{x}^2} + \frac{g l_c}{u_c^2} \qquad [15]$$

$$\frac{l_c}{t_c u_c}\frac{\partial \overline{T}}{\partial \overline{t}} + \overline{u}\frac{\partial \overline{T}}{\partial \overline{x}} = \frac{1}{Pe}\overline{\alpha}\frac{\partial^2 \overline{T}}{\partial \overline{x}^2} + Da\frac{\overline{Q}}{\overline{C_p T_c}}\overline{\dot{w}''} \qquad [16]$$

$$\frac{l_c}{t_c u_c}\frac{\partial \overline{y_i}}{\partial \overline{t}} + \overline{u}\frac{\partial \overline{y_i}}{\partial \overline{x}} = \frac{1}{LePe}\overline{D}\frac{\partial^2 \overline{y_i}}{\partial \overline{x}^2} + Da\frac{I}{y_{ic}}\overline{\dot{w}''} \qquad [17]$$

$$\frac{\partial \overline{T}}{\partial \overline{t}} = Fo\overline{\alpha_s}\frac{\partial^2 \overline{T_S}}{\partial \overline{x}^2} \qquad [18]$$

Equations [15-18] gives the normalized form of the governing equations for the gas and solid phase. Large power systems have large characteristic lengths and generally the Reynolds (Re) and Peclet (Pe) numbers are also large. Thus the fluid flows are mostly turbulent, and as seen from Equations (15 -18) the viscous and diffusive effects are small compared to the convective effects. It is also deduced that the characteristic time in these convective dominated flows is

$$t_c = \frac{l_c}{u_c} \qquad [19]$$

which is normally referred to as the residence time, [15]. As the size of the devices become smaller, the character of the governing equations and the importance of the different terms in the equations change. As the characteristic length of the device is reduced, the Reynolds and Peclet numbers decrease and fluid flow tends to be less turbulent, so the viscous effects and the diffusive transport of mass and heat become increasingly important. From the combustion stand point , an important issue is the magnitude of the residence time, because it as the scale decreases, the magnitude of the residence time also, and it always has to be larger than the chemical time for complete combustion.

For MEMS devices the flow is primarily laminar. As seen from equations (15 – 18), the viscous and diffusive effects dominate while the convective effects become negligible. So the characteristic time becomes:

$$t_c = \frac{l_c}{u_c} Pe = \frac{l_c^2}{\alpha_c} \qquad [20]$$

also called the diffusion time. Species mixing would primarily be done by diffusion as the flow is primarily laminar and turbulent mixing is very small. This makes diffusion time important as it has be lesser than the residence time in order to have complete combustion.

Fourier number characterizes thermal diffusivity in the solids and it is given by

$$Fo = \frac{\alpha_{sc} t_c}{l_c^2} \qquad [21]$$

Fo increases as the length scale is reduced. The characteristic time of the heat conduction in solids is given by

$$t_{sc} = \frac{l_c^2}{\alpha_{sc}} \qquad [22]$$

The thermal diffusivity of proposed MEMS materials (typically Si, SiC) is of the same order as that of air and gas. Air at 300 K has a thermal diffusivity of 0.000024 m^2s^{-1} while thermal diffusivity of Silicon at the same temperature is 0.00008 m^2s^{-1}. This factor is important as it has implications in heat transfer behavior between gas to, or from solid especially if there are periodic heat fluxes at the boundaries with characteristic times different than the diffusion time.

It can also be deduced that as the length scale becomes smaller while having a constant wall and flow variables, the velocity gradients, wall frictional effects, gas temperature and species gradients at the wall increase. In micro devices it's tough to keep flow velocities, temperature and mss concentration differences or the same magnitude as compared to larger devices.

4.2 Fluid flow in micro devices

Typically, Reynolds number characterizes fluid flow in most engineering applications. In micro scale devices Re is relatively small. This is due to the smaller channel cross sectional areas for fuel intake, exhaust and in micro combustors the actual size of the combustor. As computed in [15], for a 100 W meso-scale device using a stoichiometric mixture of octane/air and with a system efficiency of 10%, the volumetric flow rate of gaseous mixture to be 0.4 l/s and assuming a 5 mm diameter intake tube, the Reynolds number will be of the order of 5000 or below, depending on the gas temperature. Similarly, for a 100 mW micro-scale device with a 0.5 mm diameter intake, the Reynolds number will be around 50. Since below 5000 is considered laminar, the mixing of species would take place primarily by diffusion.

Frictional losses in the channels would be high due to viscous effects and the large aspect ratio of the micro-channels. This is experimentally studied in detail in Chapter 6. But on the other hand, the high viscous forces can help reduce the leakage through moving interfaces. This factor becomes increasingly important in internal combustion engines like the IC WDE, as their efficiency is dependent on the compression ratio.

Like macro scale combustion, even at micro scale, ambient air is the source of oxygen for hydrocarbon fuel combustion. The fuel must be vaporized and mixed with the air prior to entering the combustion chamber or the microchannel in premixed system or have direct injection in non premixed combustions systems. Previous studies have observed that the phase change in a micro scale channel takes place suddenly an in an unstable way, [17]. This could be due to the large surface area to volume ratio in micro-channels that enhances the nucleation and wetting effects at the wall, and to the behavior of bubbles that is strongly affected by the small length scales and significantly differs from macroscopic behavior, [15]. Atomizing the fuel before it is injected into the combustion chamber is a solution to increase fuel evaporation. But this adds the pressure and energy requirements on the system. MEMS scale atomizers have been developed, [18] but more sophisticated devices would be needed to produce micron size droplets that will evaporate and mix with the air in the available micro-scale residence time, [19].

Mixing is an issue in the micro scale combustion, with diffusion causing the major part of the mixing. But since the residence time of the mixture is really small, diffusion alone may not be sufficient to cause proper mixing. Different dynamic approaches like flow instabilities and ultrasound, [20, 21] may have to be implemented but this leads to fabrication and design complexities.

4.3 Thermal and heat transfer issues in micro-combustion

As the characteristic lengths are decreased the temperature gradients become higher. This makes heat transfer by conduction through the gas to the surrounding surfaces and by forced convection in the intake and exhaust channels and in the combustion chamber a significant issue. In micro-scale devices the surface to volume ratio is high, which combined with enhanced heat flux, results in heat transfer effects becoming very important at the surface or boundaries. This is a disadvantage for combustion chambers or channels as it deters their performance due to surface heat losses and wall quenching.

Heat flux from the flowing hot gases in the combustor channel to the ambient air can be computed using this simple 1-D steady state computation

$$\frac{q}{A} = \frac{T_g - T_a}{\frac{1}{h_g} + \frac{l_c}{\lambda_s} + \frac{1}{\frac{\lambda_a}{l_c} + h_{ra}}} \qquad [23]$$

From equation 23 we see that large thermal conductivity of the structure (SiC) the solid conduction terms is very small and negligible at these small scales, also conduction through air is small compared to radiation.

Preheating the mixture will help in sustaining combustion in lengths smaller than quenching distance but it may also result in auto ignition at the inlet port. Also, preheating reduces the mass charge density of the incoming charge thus reducing the potential net power output of the device.

Because of the small size, most micro devices operate at a relatively uniform temperature. Due to this reduced thermal gradients, we have reduced thermal expansion stresses and subsequent misalignments in moving parts.

4.4 Combustion at micro-scale

The basic condition for combustion to take place at a micro scale is that the physical time available for combustion, also called the residence time must be larger than the time required for the chemical reaction to occur i.e. combustion time. In case of closed systems like the internal combustion engines, the size of the chamber as well as the rpm of the engine determines the residence time. For micro scale combustion, small chemical times are needed which could be attained using high combustion temperatures. This can be achieved by minimizing heat losses, pre increasing the reactants temperature, using stoichiometric mixtures or by using high energy fuels which might be a bit more expensive.

Due to a decrease in combustion volume and scale, the surface to volume ratio increases which increases the surface heat losses and causes the waste of radical species at the wall. These factors could lead to quenching and various thermo chemical techniques like the use of excess enthalpy combustors, having insulated temperature boundary condition, establishing high temperature ceramic walls and using surface coatings, [23, 24, 22] could help overcome quenching.

Higher operating temperatures of the combustion channel walls helps reduce the chemical time and thus reduce quenching [15]. Ceramic materials like SiO_2, SiC, Si_3N_4, can withstand temperatures of around 1700K and this makes them an excellent candidate for micro combustion or micro channel materials. Also the smaller size and compactness reduces the chances of fracture.

The quenching distance magnitude reported in the literature is considered often as the limiting scale for micro-scale combustion. "This is a conceptual error, because the quenching distance depends on the reaction rate, and thus on the temperature, species and radical concentration (it is related to heat and radicals losses to the wall). The problem of wall quenching can be reduced or prevented by increasing the wall temperature (the quenching distance is approximately inversely proportional to the square root of the temperature), or equivalently preventing the heat losses to the wall (adiabatic wall)", [15].

Additional time and volume would be needed for fuel evaporation and mixing if the fuel is not premixed and if the fuel is liquid. This is an important factor since we are moving towards miniaturization. As compared to the gaseous premixed residence time, the time can be more because of the evaporation and less mixing due to smaller Reynolds number.

Some interesting alternatives to spray combustion are been researched. They include the concept of burning the liquid fuel while forming a liquid film along the wall of the combustion chamber or channel, [25]. The wall film reduces heat losses from the combustor (a channel in our case) as it keeps the combustor walls at a lower temperature (liquid boiling point), while reducing wall quenching.

While designing for micro combustion one should realize that although the increase of the surface to volume ratio of the channel or the combustor favors catalytic combustion over gas phase combustion. "Although the catalytic reaction is generally slower than the gas-phase reaction, and surface heat loss is a problem that also affects the catalytic reaction. The relative increase of surface area and the lower temperatures of the catalytic reaction suggest that micro-scale combustors using catalytic reaction may be easier to implement than those using gas-phase reactions", [15].

The potential solutions for the shorter residence times and lower temperatures could provide us with some operating models but a more thorough understanding of low temperature chemical kinetics is needed. Development of highly energetic reactive fuels could also help achieve this goal.

Even though the field of micro scale power generation by using combustion is relatively new, different research groups around the world are well advanced and the state of art is available widely. Some of them are shown below

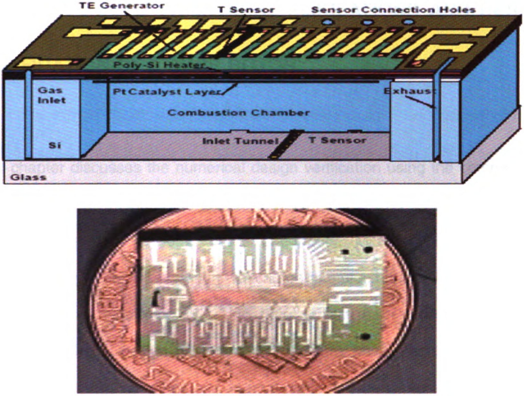

(a)

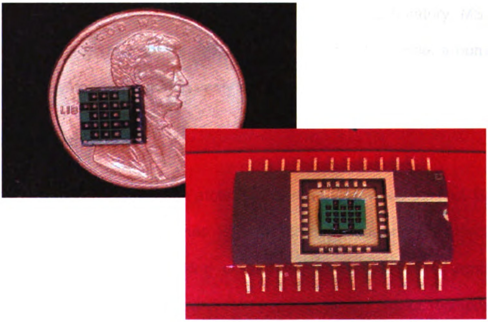

(b)

Fig 79 (a) Integrated catalytic combustor-thermoelectric micro power generator, [26], (b) MEMS fabricated array of "Digital-Propulsion" micro-thrusters, [27]

CHAPTER 5: 2-D NUMERICAL SIMULATIONS AND DESIGN VERIFICATION OF A WAVE ROTOR

This chapter discusses the numerical design verification using the commercially available Computational Fluid Dynamics (CFD) software FLUENT®6.2. The researchers at the Turbomachinery Laboratory, Michigan State University College of Engineering have been working on manufacturing a Wave Rotor Test Rig, a California department of energy grant project. As a part of this project, a universal analytical design procedure for pressure wave machine or the wave rotor to enhance gas turbines and internal combustion engines in a topping or a bottoming cycle has been developed. This is done by Ludek Pohorelský and Pranav Ajit Sane, two researchers at the Turbomachinery Laboratory, MSU. As verification for the porting angles, which were a result of this code, a numerical solution was developed in order to verify the results.

5.1 Wave Rotors

Unsteady flow devices have been around for a while and widely studied. But the design process of such machines is quiet complicated and intensive. The dynamic pressure exchange taking places due to unsteady flow conditions causing pressure wave and expansion waves yields higher compression efficiencies and also improves the overall efficiency. The construction of a wave rotor involves an array of channels arranged around the axis of a hollow cylindrical drum. As shown in figure 25 , this channel drum rotates between two stationary end plates or in some designs the end plates rotates around the stationary rotor. Depending on the design and type of cycle each endplate has a few ports or manifolds, controlling the fluid flow through the channels. As the rotor rotates or vice versa, the channel ends are periodically exposed to differing port conditions like pressures and temperatures, initiating compression, and expansion waves within the wave rotor channels.

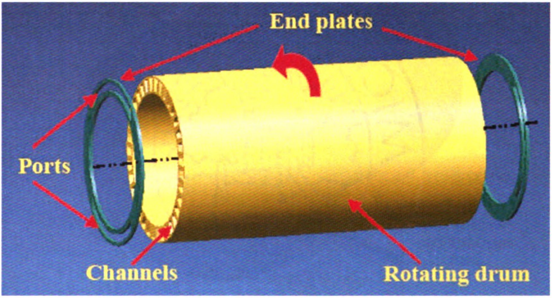

Fig 80 Schematic showing the rotor and ports, [6]

The number of ports and their positions depend on the type of applications and flow conditions and thus has to be computed precisely for each specific application. By carefully selecting their locations and widths to generate and utilize wave processes, a significant and efficient transfer of energy can be obtained between flows in the connected ducts. Thus, pressure is exchanged dynamically between fluids by utilizing unsteady pressure waves. Wave rotor accomplishes compression and expansion within a single component as compared to the steady flow turbomachines. Since such devices are very sensitive to back pressures, the port timings are very crucial. Also to reduce leakage the gap between the channels and the end plate has to be minimal but without contact with the rotor under all operating and thermal expansion conditions.

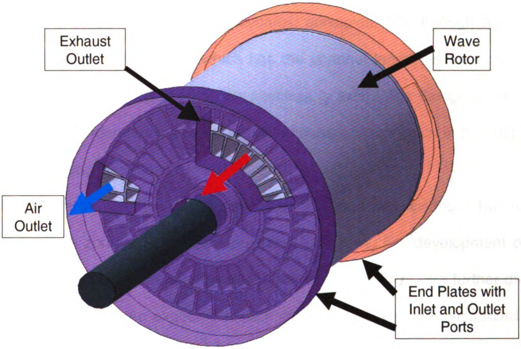

Fig 81 A 3 D model developed in Catia to model the wave rotor test rig. Showing the arrangement of face plates and rotor over a shaft, [28]

The figure shows a 3 D model of the wave rotor and face plates assembly over the shaft. The wave rotors have two basic flow configurations, through flow and reverse flow. This project has been based on the through flow design as shown in this figure with air outlet port and exhaust outlet. For this configuration air and exhaust gases enter from one side while the other side has the high pressure air and exhaust gases leaving the system. More details are widely available in the literature, [6,8,12].

5.2 Formulation of the Analytical code

The analytical code for the 1 D through flow wave rotor model was based on shock wave theory and linear gas dynamic principles. The through flow wave pattern is shown in the figure which has the channel length as the ordinate (x axis) and the time is projected on the abscissa (y axis). The design of porting is based on the understanding of the expected wave pattern which in turn depends on the operating conditions.

As this was a through flow configuration, the flow area was divided in two zones, high pressure zone (HP) and low pressure (LP) zone. For development of the code and for better understanding of the flow zone, this area was further divided into ten zones, [28]. An expected pattern of wave flow has been visualized they have been explained.

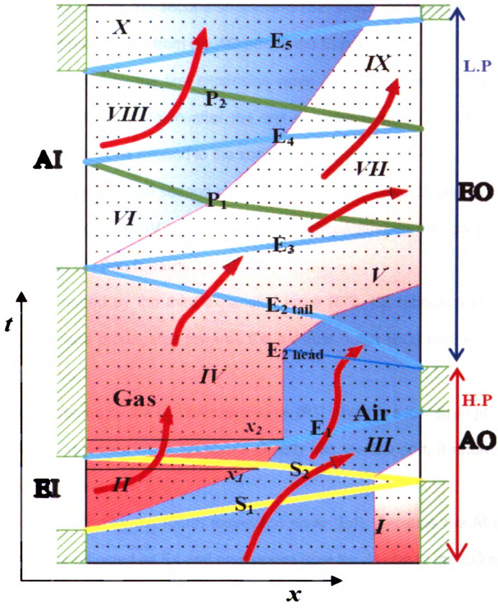

Fig 82 Wave Patter in a through flow wave rotor configuration, [28]

I - Zone of the rotor filled with ambient air or a mixture from the previous cycle. This is the initial stage of the through flow cycle.

II - Zone created by the first shockwave (S1) which propagates due to the high pressure at the exhaust inlet (EI) port and travels towards the air outlet (AO) port.

III - Zone created by the second shockwave (S2) which increases the Zone III pressure and propagates from the AO port to the EI port

IV - Zone created by the first expansion wave (E1). This zone separates the HP region from the LP region after the first expansion wave, E1. The air-gas components of the zone expand to the zone pressure due to E1.

V - Zone created by the second expansion wave (E2) which is created by the sudden opening of zone IV to the EO port. E2 propagates in the low pressure region from the EO port towards the AI port.

VI - Zone created by the third expansion wave (E3). E2 rebounds at the air inlet (AI) port and propagates towards the exhaust outlet (EO) port as a weak expansion wave.

VII - Zone created by the first pressure wave (P1) which is a low strength shock wave. As the returning wave E3 opens directly into the EO port, it returns as a weak pressure wave P1.

VIII - Zone created by the fourth expansion wave (E4). Because the AI port is still open, P1 is reflected as E4 and propagates from the AI port to the EO port.

IX - Zone created by the second pressure wave (P2) which travels from the EO port to the AI port due to similar interactions as before. Pressure and expansion waves in low pressure part are weak.

X - This zone is created by the fifth expansion wave (E5). The mixture of fresh air and exhaust gas expands through E5 to reach the same condition as the beginning of the cycle. If any exhaust gas recirculation is present from the previous cycle, it is exhausted to the AO port.

For the analytical model, the governing equations were the normal shock wave relationships and methods of characteristics expressions as developed in section 3.1.

The shock wave relationships for the pressure ratio, Πs between two zones were:

$$\pi_S = \frac{p_{behind\ shockwave}}{p_{ahead\ of\ shockwave}} = \frac{p_{II}}{p_I} \qquad [24]$$

The local change of temperature across two zones was given by:

$$\frac{T_I}{T_{II}} = \pi_S \left(\frac{\left(\frac{\gamma+1}{\gamma-1}\right) + \pi_S}{1 + \left(\frac{\gamma+1}{\gamma-1}\right)\pi_S} \right) \qquad [25]$$

with the local speed of sound being

$$a = \sqrt{\gamma R T} \qquad [26]$$

From there relationships we can find the induced velocity of the fluid due the shock wave is

$$u_S = \frac{a}{\gamma}(\pi_S - 1)\sqrt{\frac{2\gamma/(\gamma+1)}{\pi_S + \left((\gamma-1)/(\gamma+1)\right)}} \qquad [27]$$

and the shock wave velocity is given by

$$w_s = a\sqrt{1 + \left((\gamma+1)(\pi_S - 1)/2\gamma\right)} \qquad [28]$$

The assumptions behind this code were

- Isentropic flow behavior
- No heat transfer through the walls
- Fixed initial pressure and temperature at the start of the cycle
- Flow direction to be normal to the ports
- No leakage

This made us achieve higher than practically possible results but gave a quick method to develop the porting design.

According to the code, the following porting angles were arrived by using the following boundary conditions:

P1: Pressure of fresh air at AI: 0.995 bar

P2: Pressure of compressed air at EO: 1.88 bar

P3: Pressure of exhaust gas at EI: 1.5 bar

P4: Pressure of exhaust has at EO: 1.01 bar

Boundary conditions for temperatures were:

T1: 300 K

T2: 600 K

Computed temperatures were:

T3: 1100 K

T4: 860 K

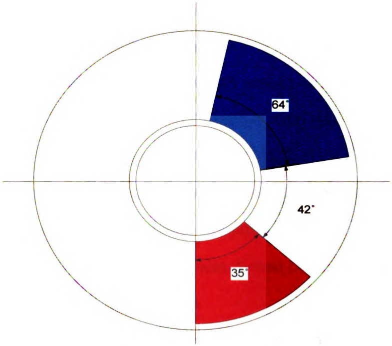

Fig 83 Inlet Side plate, Blue showing air inlet (AI) and Red showing exhaust inlet (EI)

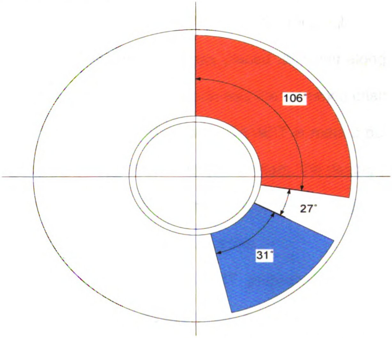

Fig 84 Outlet side, orange showing the exhaust gas outlet (EO) and blue showing the compressed air outlet (AO) angle

Figures 28 and 29 showing the porting angles which were used to develop the 1D code and 2D simulations.

5. 3 Development of the CFD Model

For the development of the CFD model, this porting geometry was used. This was laid out on a 2D plane. The length on the rotor was computed from the average radius of the rotor, 36 mm and the total length of the channel were taken to be 113 mm. This was divided into 24 channels of 5 mm width each with the wall thickness taken to be approximately 0.5 mm. The length of the channels was 93 mm. The leakage was 0.25 mm and was divided between the face plate and the rotor plane, at 0.125mm on each side.

The technique used was straight forward. For the rotor channels, a large rectangle (113 x 93.25) was made and then another rectangle of 0.5 x 93mm placed in the middle. By default GAMBIT places this rectangle at the origin. Now this smaller rectangle (wall thickness) was placed 26 times along the length of the bigger rectangle at a gap of 5mm which was the assumed channel thickness. Please note that the default unit of scale in GAMBIT is meters but since we will later be scaling the model in FLUENT into millimeters, the description given here is in mm's. These channels are then subtracted from the bigger area to give us channels and a 0.125 mm leakage on both sides.

The mesh was developed on the FLUENT preprocessor, GAMBIT. For the meshing, pave style technique was used, with the interfaces being much finer as compared to the center of the channel.

The operation modeled is a periodic process. For this, prior to the meshing, the periodic edges on the left end plate, rotor channel, and the right end plate were first linked. After meshing, appropriate boundary conditions were given. For the periodic boundary conditions, the two linked edges have to be selected together and assigned the periodic boundary condition. When giving the interface boundary condition, we just have to be careful while naming, as a mistake while selecting the interface in FLUENT could give us errors.

The EI and AI were given the pressure inlet conditions at the port edges and the port length corresponded to the porting angles given by the analytical code team, Pranav and Ludek, reference. The distance of the port edge to the interface was kept small as to minimize the pressure drop across that distance.

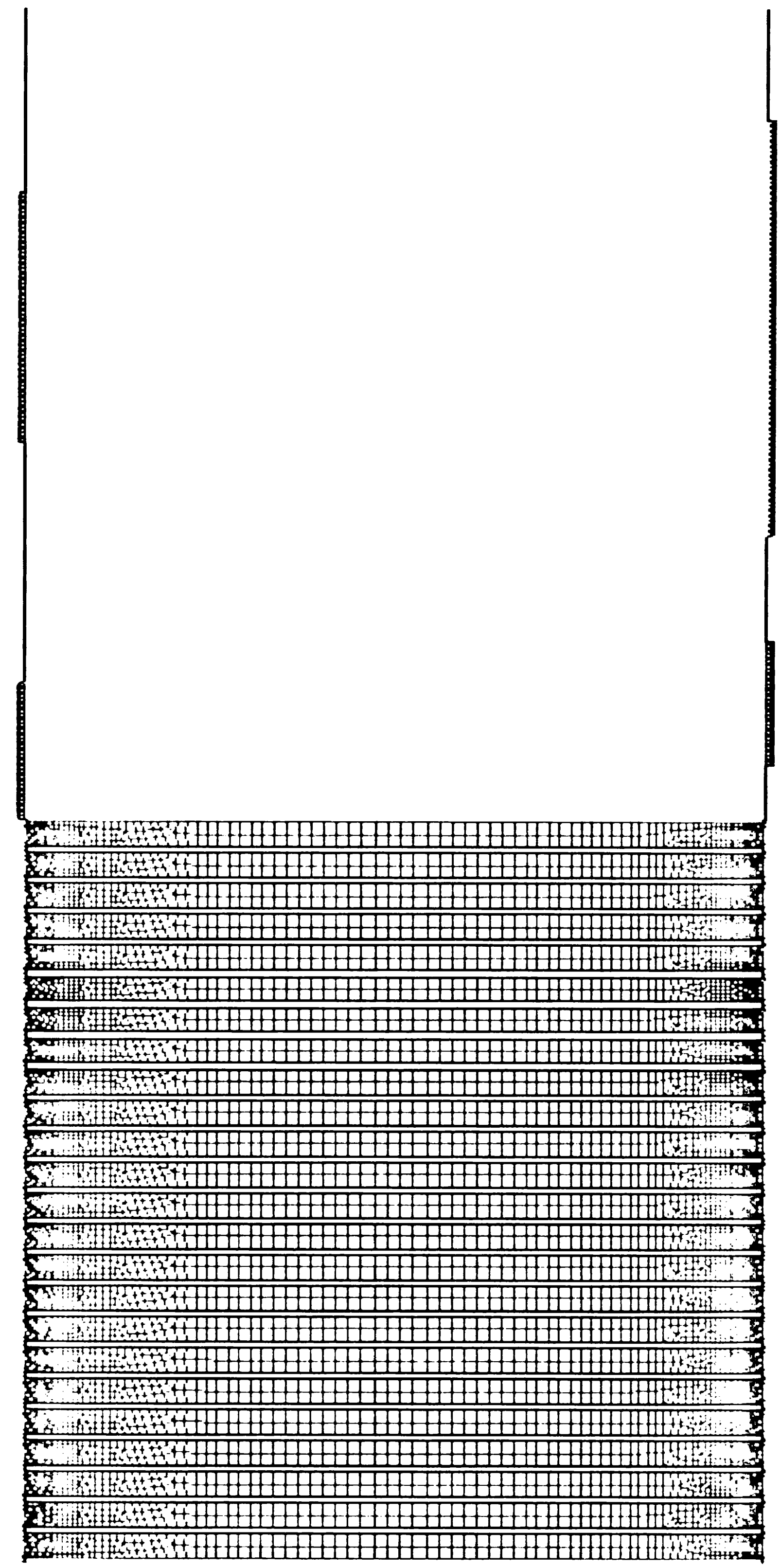

Fig 85 A 2D grid showing the channels and the porting.

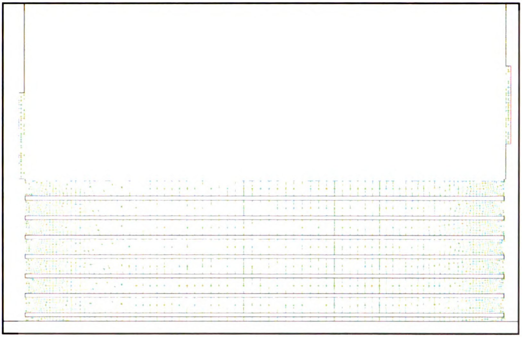

(a)

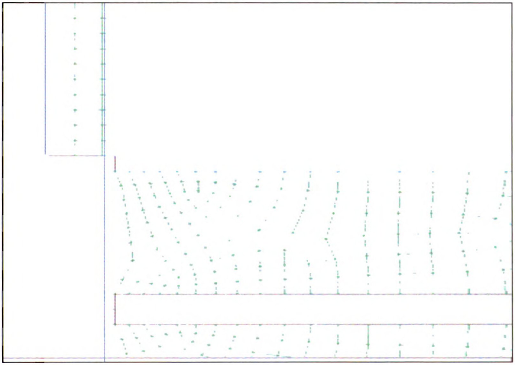

(b)

Fig 86 (a) & (b) showing the mesh entry and the leakage area

5.4 Setting up FLUENT simulations

This grid was then exported to FLUENT solver. A 2D double precision solver was chosen. The grid was scaled to the millimeter scale. FLUENT is arranged in such a scale as to go from left to right in order. An unsteady flow, 1st order upwind scheme with coupled energy equation was selected. Since the analytical model did not account for viscous effects, an inviscid model was chosen for the formulation. The boundary conditions were chosen as per the analytical model. The interfaces were defined as a couple.

The rotor mesh was a moving mesh and had to be given a 'y' velocity. This was computed using the average radius and the rotational speed at which the analytical model was computed. They were 39 mm and 13,000 rpm respectively and the y velocity was computed to be 49 m/s.

For the solution, a PISO solver was selected. PISO stands for Pressure Implicit Splitting of Operators. This is recommended for time dependent problems like this. The solution was initialized at the ambient conditions prescribed in the analytical model. The four ports were then 'patched' by the initial temperatures and pressures for cycle initialization.

The time step was chosen based on the commonly used Crank Nicholson Scheme for Implicit solutions. 10 E-6 was the time step at which different computations was performed.

5.4 Numerical Results

After about 30 cycles, a steady state solution was expected and is presented. Contours of static and total pressures along with temperature profile showing clear recirculation is shown.

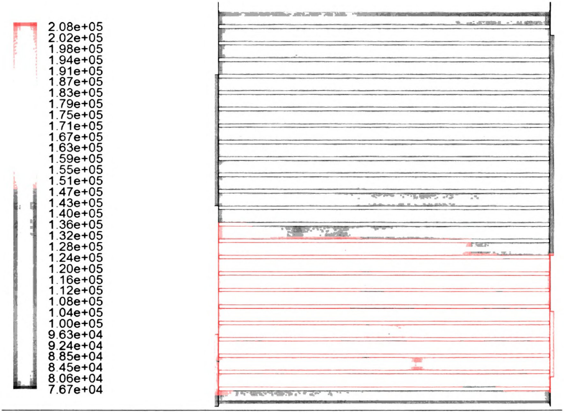

Fig 87 Static pressure (pascals) contours showing the wave pattern in a through flow configuration

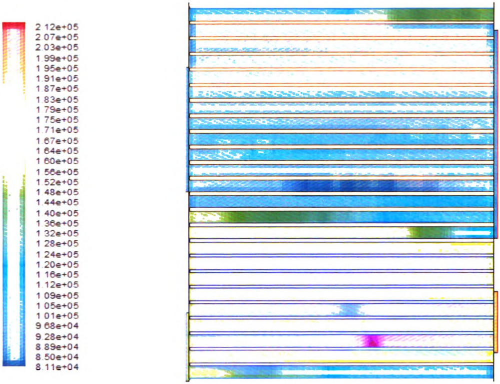

Fig 88 Total pressure (pascals) contours showing the wave pattern in the channels

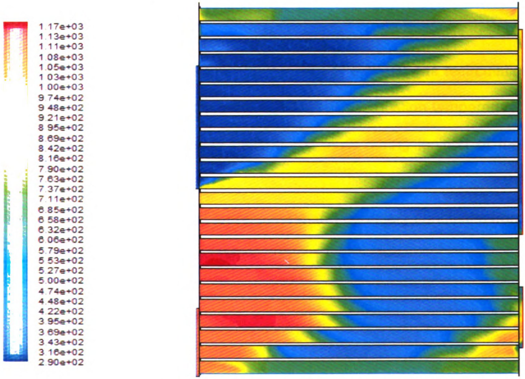

Fig 89 Static temperature profile showing the flow pattern and the exhaust gas recirculation in the exhaust outlet, EO

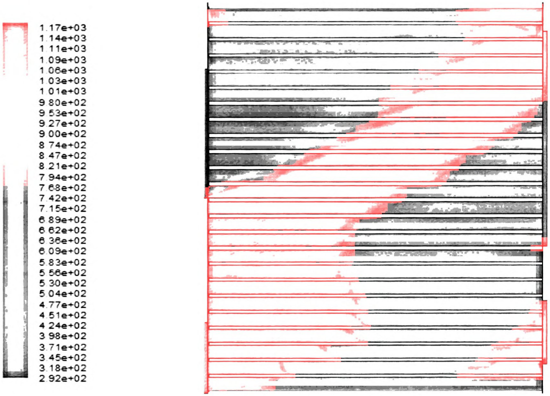

Fig 90 Total temperature profile showing the flow pattern and the exhaust gas recirculation in the exhaust outlet, EO

The area near the exhaust outlet shows the area of exhaust gas recirculation. It could decrease the emission NOx because of lower combustion temperature, but on the other side, lack of oxygen causes problems during ignition of fuel air mixture.

The wave pattern using the exact same porting and boundary conditions from the MATLAB analytical code is shown below.

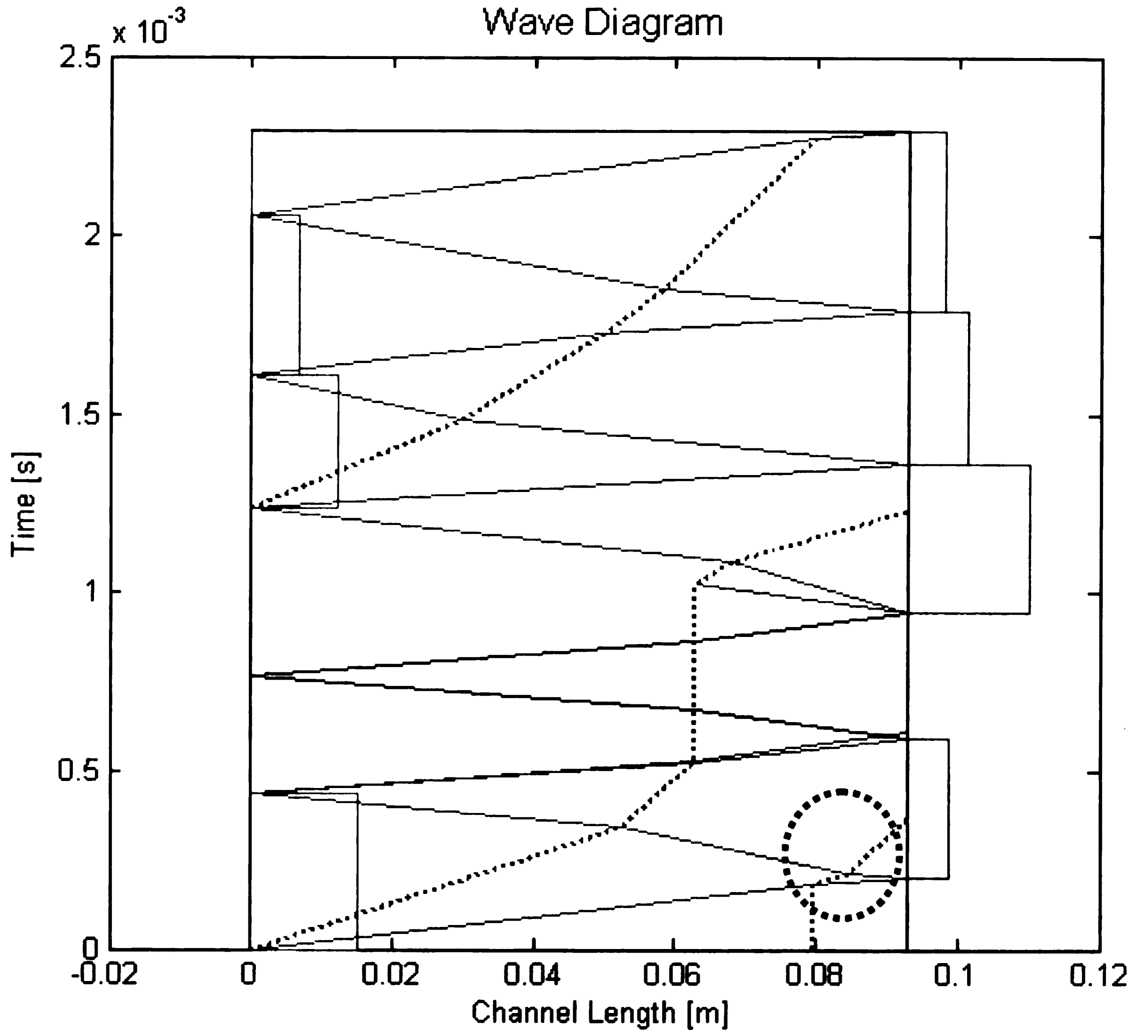

Fig 91 1 D Analytical model results showing the wave behavior , the red dots showing the gas air interface and the green traces showing the net flow velocities, [28]

This figure shows a very good comparison between the analytical and the numerical code wave pattern.

Now for another comparison, and to see the flow behavior, we will compare the x velocities at different port, with the ones developed by the 1 D analytical code developed in MATLAB.

The results are shown next:

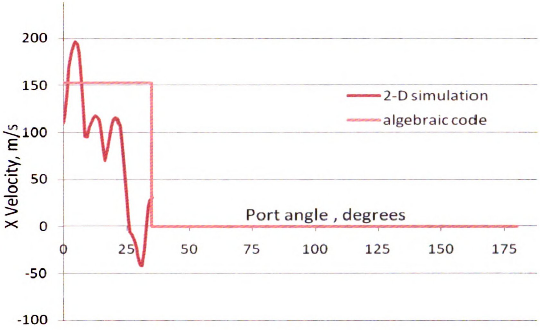

Fig 92: X velocity comparison of the Exhaust Inlet Port

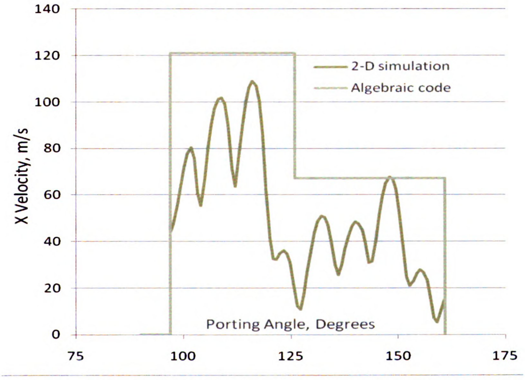

Fig 93: X velocity comparison of the Air Inlet Port

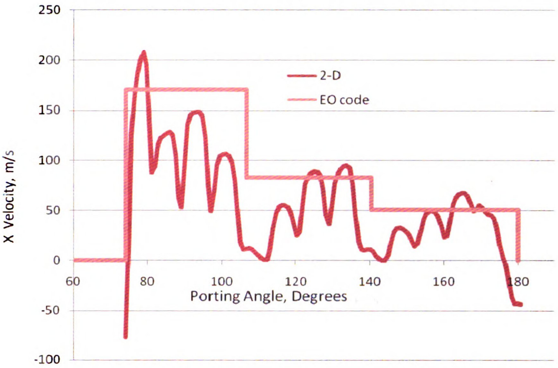

Fig 94: X velocity comparison of the Exhaust Outlet Port

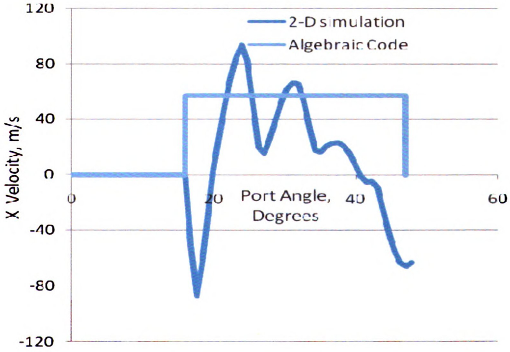

Fig 95: X velocity comparison of the Air Outlet Port

The result shows a correlation. Since the FLUENT model is more precise, and has more data points it gives a nice curve where as the algebraic model shows linear behavior. The channel walls can be accounted for the erratic behavior as shown by the FLUENT results.

Figure 37 shows the X velocity pattern over the exhaust inlet length. It also captures some back flow into the port; this might be caused due to the leakage. The flow behavior is depicted in the figure below. The vectors plotted here are the velocity magnitude and should be interesting to see how they compare with the X velocity plots. Near the top edge of the port some circulation is clearly visible.

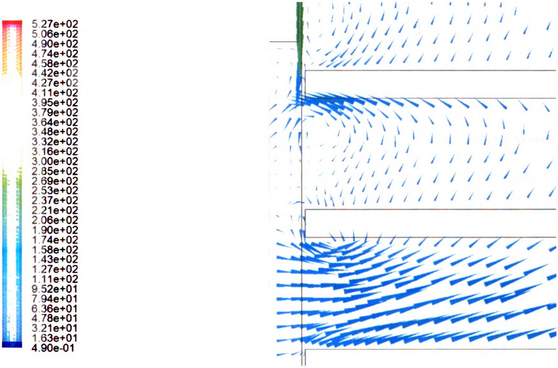

Fig 96: Velocity magnitude vectors showing the backflow in exhaust inlet port

The air inlet port comparison, figure 38 shows similar results. Higher X flow velocity near the beginning of the port but it steadily falls down as the port is closing. Figure 39 shows a close correlation between the two results. The flow velocities steadily decrease across the Exhaust Outlet Port. Strong exhaust gas recirculation is visible across the edges of the Air Outlet port in figure 40. This is seen from the negative x velocities, showing the flow going back into the channel.

5.5 Approach for modeling the Wave Disc Engine

The techniques from the wave rotor simulations can be extended to develop the wave disc engine CFD model. As a wave disc engine also has periodic unsteady flow, the same principle can be applied for modeling. There are just 2 ports involved in the WDE engine design so that makes it less complicated than the wave rotor. The most challenging task would be to model combustion in a rotating channel, periodically.

For now, combustion can be modeled as sudden heat addition (sudden pressure rise) in the channel. A more precise geometry could be developed in AutoCad and imported in GAMBIT. In a more sophisticated approach, the channels could be curved or in the form of spiral. This will increase the channel length. The curved channel with greater lengths and different angles at inlet and outlet can be used to extract work and self propel the disc. The varying angles at the inlet and the outlet have to be precisely computed and modeled. The channel could also be inclined at an angle with respect to the radii. Some of the different disc designs and the variation of channel angle is shown in the figure 42 below.

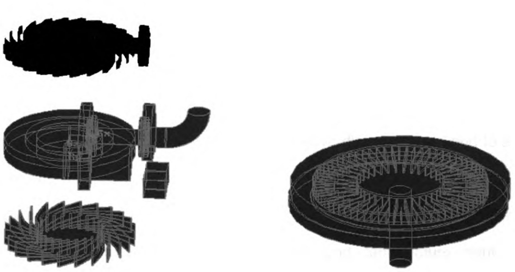

(a)

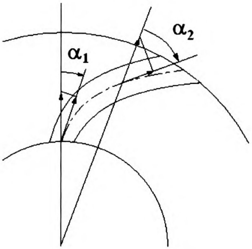

(b)

Fig 97 (a) Examples of some wave discs, (b) Curved channel variation, [14]

The progression of compression and expansion wave can be simulated in exactly the same way as done for the wave rotor. Modeling of combustion taking place periodically in a rotating channel should be a much more intensive task. The porting can be fine tuned using the flow pattern and the rotational speed of the disc.

CHAPTER 6 : PRELIMINARY ANALYTICAL RESULTS FOR WAVE DISC ENGINE

To develop a preliminary understanding of the wave disc flow cycle and to arrive at a possible first porting design, an analytical approach was used. This was done by modifying the wave rotor code for the wave disc engine. Since the most significant unknown would be the pressure and temperature right after combustion, a whole range of pressures and temperatures were used to develop an understanding of the flow pattern. The pressures ranged from 2 – 20 bar and the temperatures were assumed from 700 – 2000 K. By calculating the induced flow velocities at every expected compression and expansion state, an estimate was made of the pressure and temperature range within which we could reasonably move further in our design.

6.1 Results and Discussion

The results presented below show the patterns of induced flow velocity at different compression and expansion states, and their behavior at different temperatures and pressures.

In Up'x', the x signifies the particular zone in which the wave travels. This is shown in figure 43. Similar approach has been used to develop the low pressure part of the wave rotor.

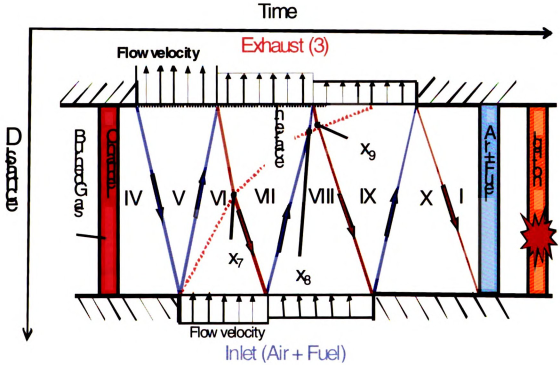

Fig 98 Wave pattern on Time v/s Distance plot

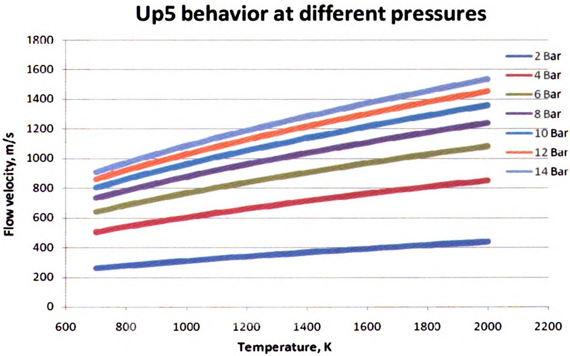

Fig 99 Temperature and Up5 velocity distribution for various pressures

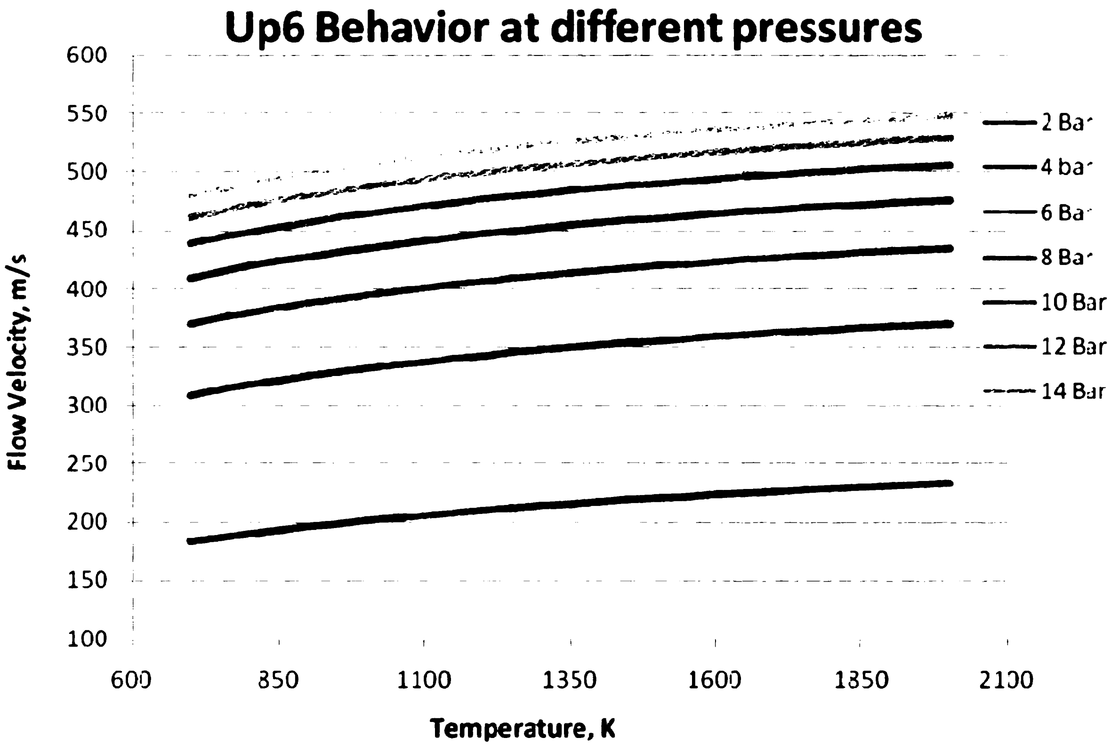

Fig 100 Temperature and Up6 velocity distribution for various pressures

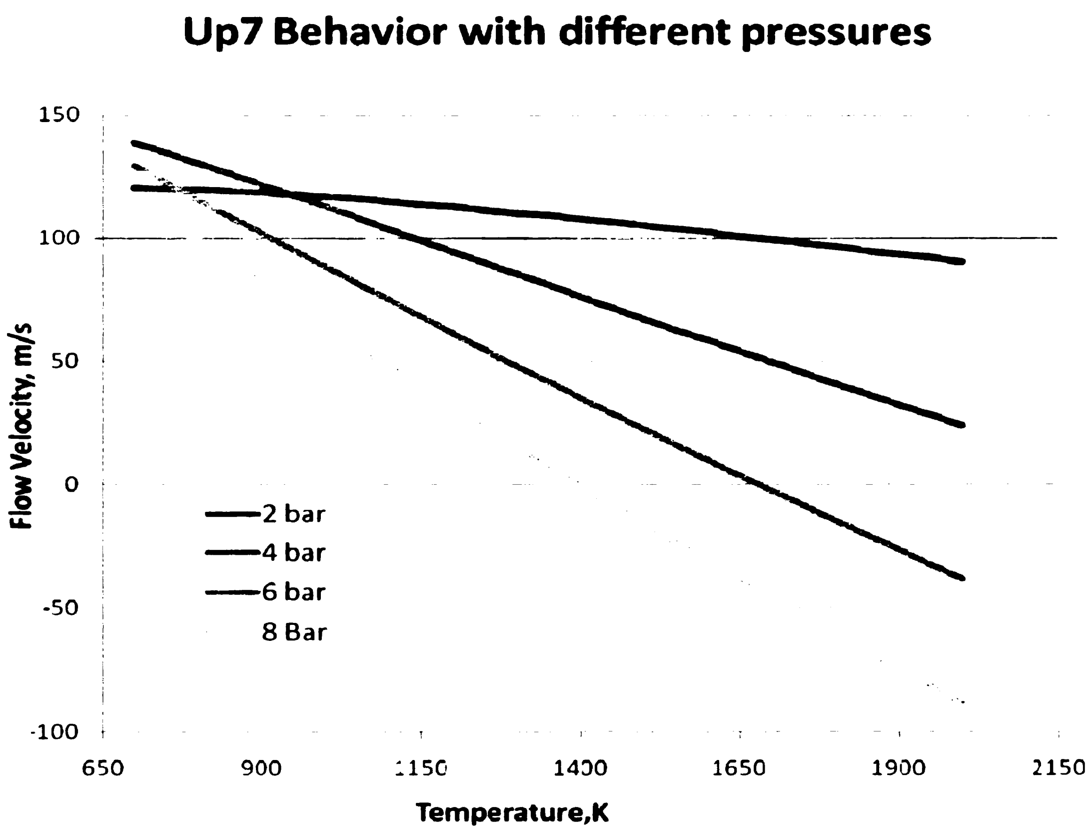

Fig 101 Temperature and Up7 velocity distribution for various pressures

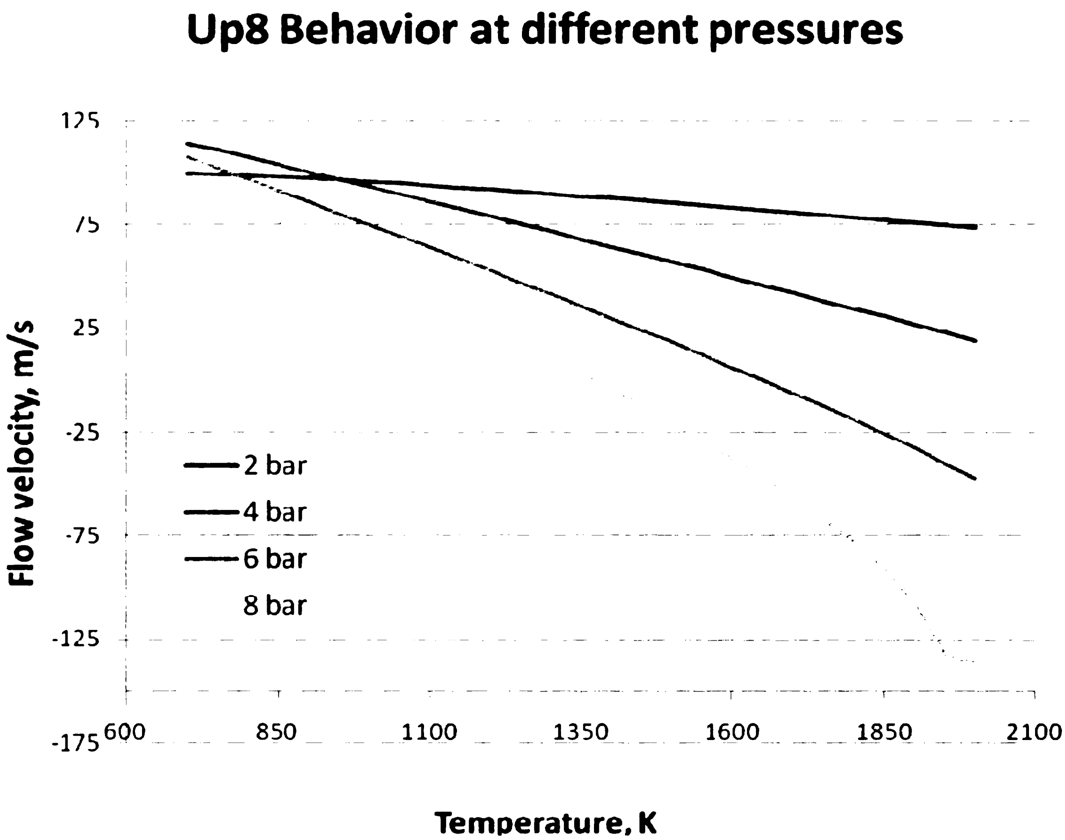

Fig 102 Temperature and Up8 velocity distribution for various pressures

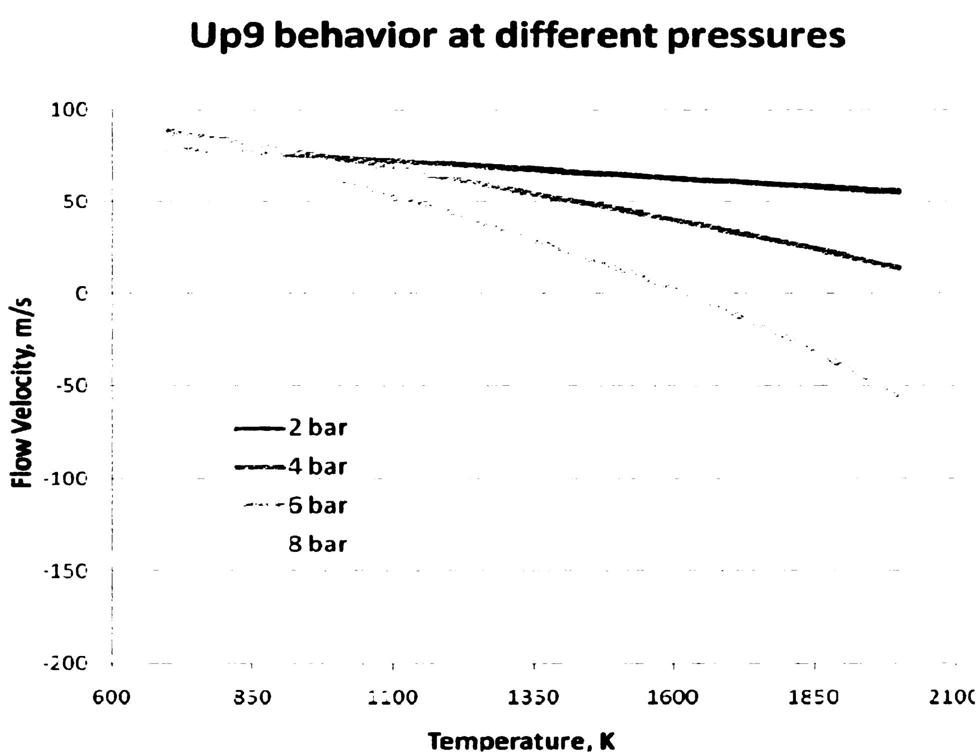

Fig 103 Temperature and Up9 velocity distribution for various pressures

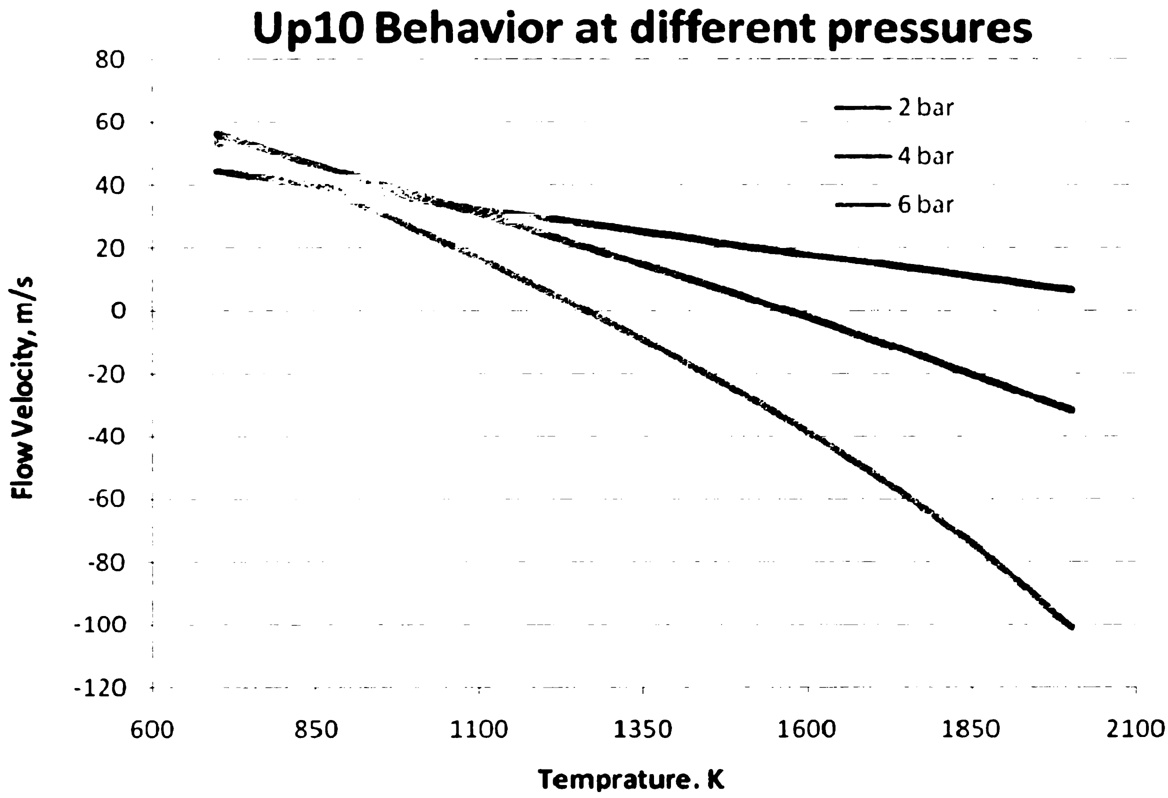

Fig 104 Temperature and Up10 velocity distribution for various pressures

The idea of this exercise was to arrive at an intelligent approximation of pressure and temperature range after combustion and also to understand how the flow velocities in AI and EO ports react to the change in these conditions. Up5 values were expected to be highest as it's induced by the strongest expansion wave E1. While observing Up5 and Up6 at pressures ranges 2-8 bar, and temperature range from 800–1400K, the flow velocities ranged between 200 to about 1000 m/s. Before arriving at conclusions we must understand that this code did not take into account the work extraction of the system. Nevertheless such high velocities seemed unrealistic and the range of interest was further narrowed down. Higher than 8 bar pressures were neglected as the constant volume combustion at such small scale might not produce pressures of that magnitude.

Also, such high pressures will increase the probability of leakage between the disc and the ports.

Observing Up7 and Up8, figure 46 and 47 we see a drastic loss in the net flow speeds due to exhaust. For higher temperatures, above 1400 K we see negative velocities, thus suggesting that to prevent backflow, port has to be closed or perhaps we can neglect the possibility of having higher than 1400 K temperature arising in a micro channel. Another observation we see from this plot is that 2 bar flow velocities are significantly lower than the 4 bar and 6 bar velocities for about 700 – 1200 K range. This could be even lower after accounting for the work extraction due to exhaust.

Narrowing down our range further to 4 and 6 bar between 800 – 1200 K range, we observe Up9 and Up10 shown in figure 48 and 49. The flow velocities show a sudden dip for 6 bar in this temperature range and while accounting for work extraction, could result in back flow in this zone.

After these observations a pressure of around 4 bars and a temperature range of 800 - 1100 K were taken to be the appropriate conditions after combustion for the preliminary design of the geometry. Now from these conditions, a gas – air interface was plotted to arrive at a preliminary porting design. Results are computed for a 2mm long channel. For the complete temperature range the interface is plotted for 4 bars and 8 bars. This is shown in figure 50 and 51.

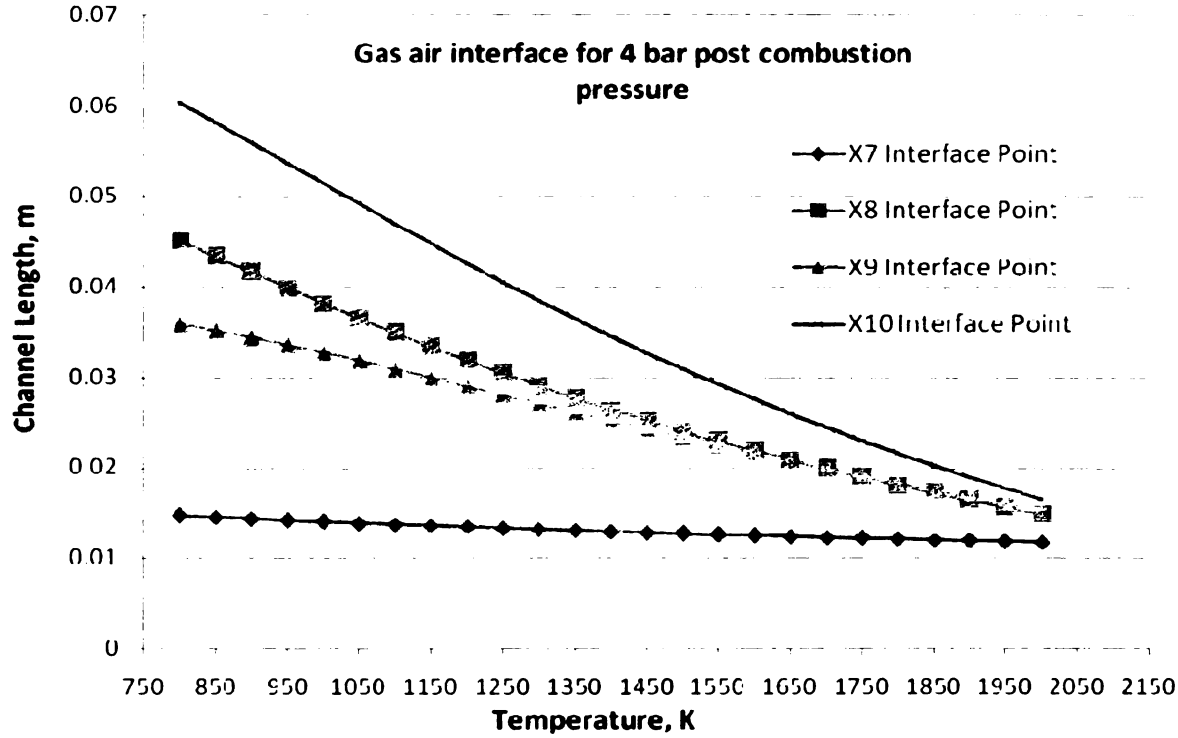

Fig 105 Gas air interface distribution for a 4 bar post combustion pressure

The interesting observation which can be made from these two plots as we can see how the interface travels within the channel for a particular range of temperatures and pressures. The channel length is 2 mm and the interfaces points for x8 and x9 are beyond the channel length up to 1950 K for a 4 bar pressure. This means that complete scavenging has already occurred and we should not be concerned about the wave reflections VII, VII, XI and X. The porting design is made accordingly.

But as we see figure 51, we see that for 8 bar post combustion temperature, we see the interfaces (or the wave reflections) takes place till about 1500 K. The directions of the interfaces shows us back flow and thus exhaust gas recirculation.

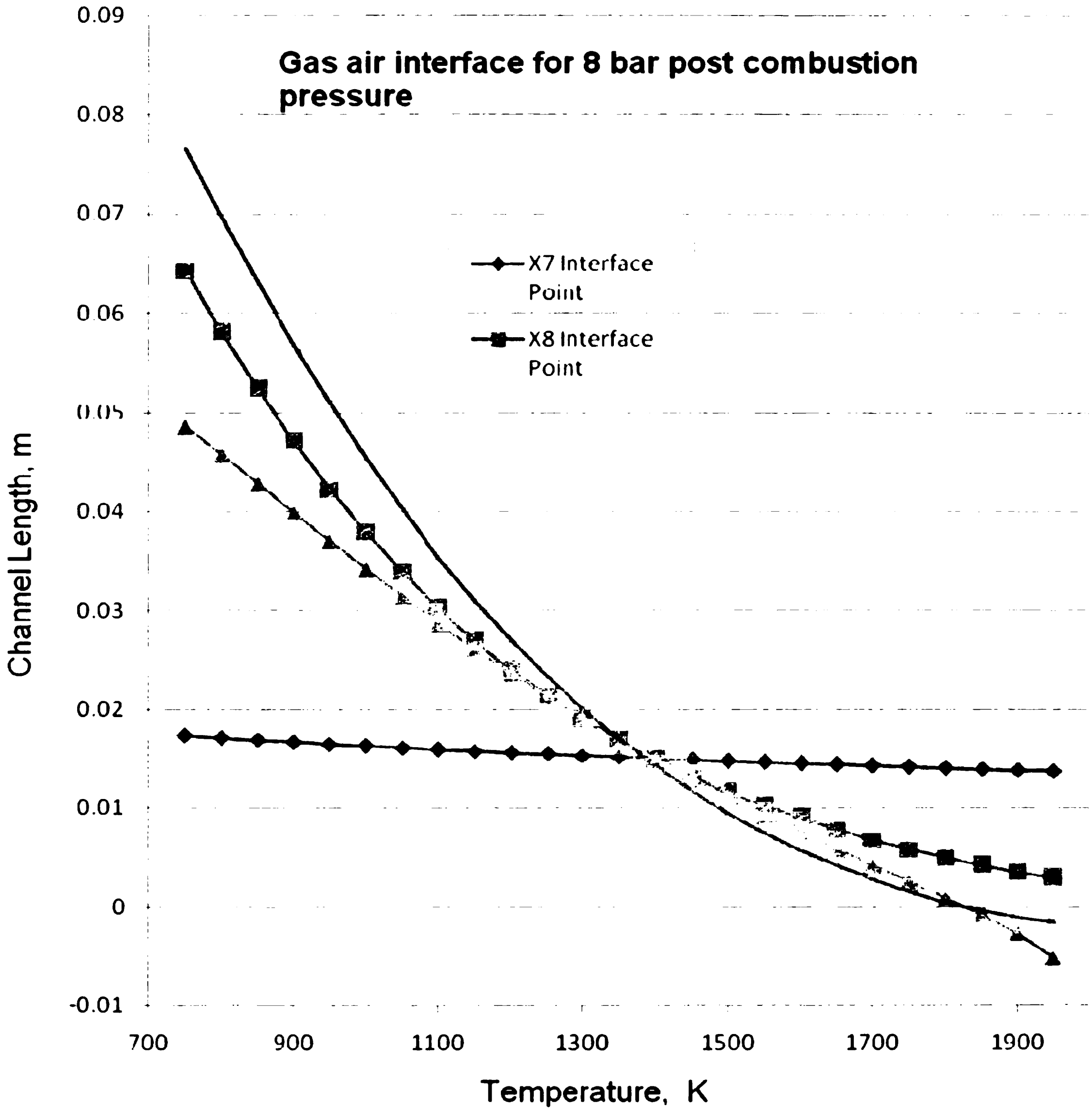

Fig 106 Gas air interface for a 8 bar post combustion temperature

While designing the porting angles we have to take in to account these factors as this will affect scavenging and chances of EGR, which in turn will affect the overall device efficiency. Centrifugal forces also affect the scavenging and a more sophisticated code should take into account of this effect.

CHAPTER 7: FRICTION FACTOR STUDIES IN MICROCHANNELS

While designing unsteady flow micro devices or MEMS, it is important to understand the flow characteristics and micro fluidic behavior. One such fluid flow characteristic is the friction factor. Friction factor calculations were preformed for three different microchannels machined inside a silicon substrate and compared with previous work. Experimental results were computed for pressure drops across micro channels with uniform rectangular cross sectional area. Channels dimensions were 3000 x 360, 1500 x 180, 750 x 90 with depth 360, all units in micrometer. Deviations of the experimental values are seen for Reynolds numbers 100 – 1000.

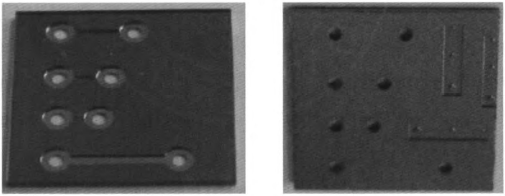

(a) (b)

Fig 107 Silicon microchannels: (a) front view, (b) back view, [8]

Figures 52 the channels machines in Silicon and topped with glass. Fig 53 shows some images taken from Scanning Electron Microscope (SEM).

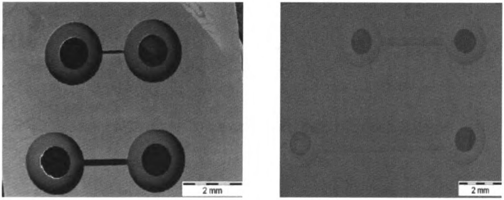

(c) (d)

Fig 108 Channels visualized with SEM: a) 90μm and 180 μm wide channels; b) 360 μm and 720 μm wide channels, [8]

Some of the first studies on friction factor were performed by Wu and Little [29] where Darcy friction factors were calculated for microchannels etched in silicon. The observed friction factors were larger than the predicted by the classical macro scale theory. The findings here verify these results as the experimental values are greater by around 22% than the theoretical values for hydraulic diameters 114μm, 240μm and 360μm. Standard properties of air were taken at one end of the channel. The temperature is assumed to be constant throughout the channel (isothermal flow). This assumption has been made considering the high coefficient of thermal conductivity of silicon, 148W/mK, although, a recent study shows no significant effect of heat transfer on the compression efficiency in silicon microchannels [8].

7.1 Theory

The two non dimensional flow parameters are often used to characterize the fluid flow are the Reynolds number Re and the Darcy friction factor f. The viscous effects of the flow are characterized by Re.

Reynolds number is given by:

$$\mathrm{Re} = \frac{\rho V_{avg} D_h}{\mu}$$

The dynamic viscosity was taken to be constant at 25 degrees Celsius.

$$D_h = \frac{4 \times A}{P}$$

The Darcy friction factor relates roughness effects to pressure drops in ducts and channels. It's defined as

$$f = \frac{8\tau_w}{\rho V_{avg}^{\;2}}$$

Using this relation and combining it with the energy and the momentum equation for the fully developed flow, the Darcy Weisbach equation is obtained, which holds for both laminar and turbulent flow.

$$h_f = f\frac{L V_{avg}^{\;2}}{D_h 2g}$$

Solving the continuity and momentum equation, the solution for the laminar flow in the Hagen-Poisseuille flow problem is found and is commonly known as the Darcy friction factor [8] as shown.

$$f = \frac{2 D_h \Delta p}{\rho L V_{avg}^{\;2}}$$

Analytically the laminar friction constants can be found out using the aspect ratio, α, which is the smaller of the ratios width/height and height/width so that $0 \leq \alpha \leq 1$.

The friction coefficient C can be represented as a function of α by the polynomial correlation

$$C = 96(1 - 1.35\alpha + 1.95\alpha^2 - 1.70\alpha^3 + 0.96\alpha^4 - 0.25\alpha^5)$$

Where

$$C = f \times \mathrm{Re}$$

The classical theory of laminar flow relates the friction coefficient to be proportional to the Reynolds number and it's given by

$$f = \frac{64}{\mathrm{Re}}$$

7.2 Experimental setup

Ambient conditions were used for the channel entry. Pressure drop across the channel was determined using the experimental set up shown in Fig. 4. The flow exit velocity was computed by measuring the volume flow rate of the water.

Estimates of pressure drops can be made using the traditional theory and correlations. However, accurate prediction of pressure drops in microchannels for non-slip flows is not yet possible [30].

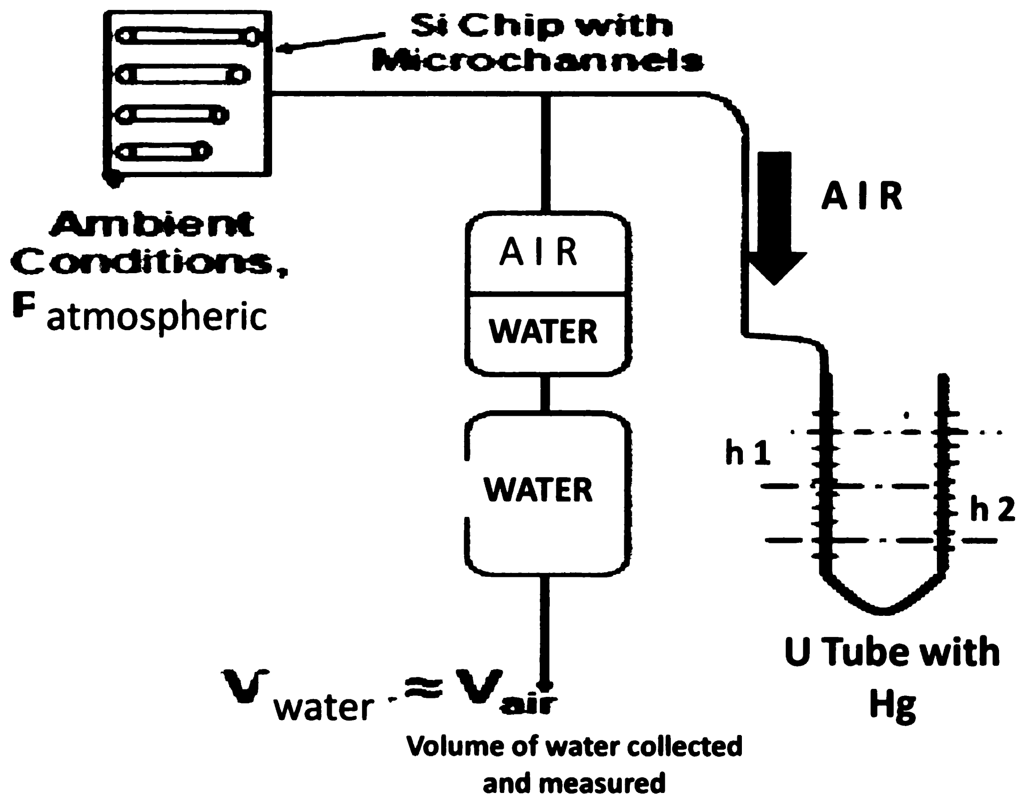

Fig 109 Experimental setup

The results for Friction coefficients C are more conveniently shown using the normalized friction coefficient

$$C^* = \frac{f\,\mathrm{Re}_{\exp erimental}}{f\,\mathrm{Re}_{theorectical}}$$

Entry and exit losses were calculated based on the standard expression for minor losses in flow. Since the port will have a dimension larger than that of the channel, the entry losses are treated as losses due to variation of diameter in a pipe. The pressure drop is

$$\Delta p = k\rho \frac{V^2}{2}$$

Where the entry loss coefficient, k is considered to be 0.5 for a contraction with sharp 90º corners [3131] . The losses were computed as head losses at entry and exit and the sharp bends using the standard minor flow losses relationships [32] as shown by the equation below.

$$\Delta h_{tot} = h_f + \Sigma h_m = \frac{V^2}{2g}\left(\frac{fL}{d} + \Sigma K\right)$$

7.3 Results

The following table gives the experimental results for the pressure drops, friction factors, normalized friction coefficients and Reynolds number for all three channel sizes.

m(kg/s) E-6	**ΔP(Pa)**	**f**	**C***	**Re**
1.147	3466	0.309	1.326	**274**
2.057	6933	0.179	1.375	**491**
2.403	8532	0.155	1.399	**574**
2.403	8532	0.155	1.399	**574**
2.859	12932	0.151	1.618	**683**
3.010	14665	0.149	1.674	**719**
3.307	17732	0.138	1.714	**790**

3.640	**21065**	**0.125**	**1.703**	**871**

Table 1: Experimental data for the smallest microchannel (750μm x 90μm x 360μm)

m (kg/s) E -6	**ΔP(Pa)**	**f**	**C***	**Re**
4.753	5466	0.090	1.344	**946**
6.369	10398	0.086	1.716	**1268**
6.409	8532	0.073	1.458	**1276**
6.608	14132	0.100	2.067	**1316**
7.519	**14532**	**0.079**	**1.851**	**1497**

Table 2: Experimental data for (1500μm x 180μm x 360μm) microchannel

m (kg/s) E-6	**ΔP(Pa)**	**f**	**C***	**Re**
9.636	7199	0.064	1.445	**1439**
8.299	5599	0.091	1.777	**1239**
6.994	4266	0.136	2.21	**1037**
5.863	**3066**	**0.208**	**2.85**	**876**

Table 3: Experimental data for (3000μm x 360μm x 360μm) microchannel

The plot in Fig. 5 shows the variation of the normalized friction factor, with different Reynolds Numbers. It is always greater than 1.

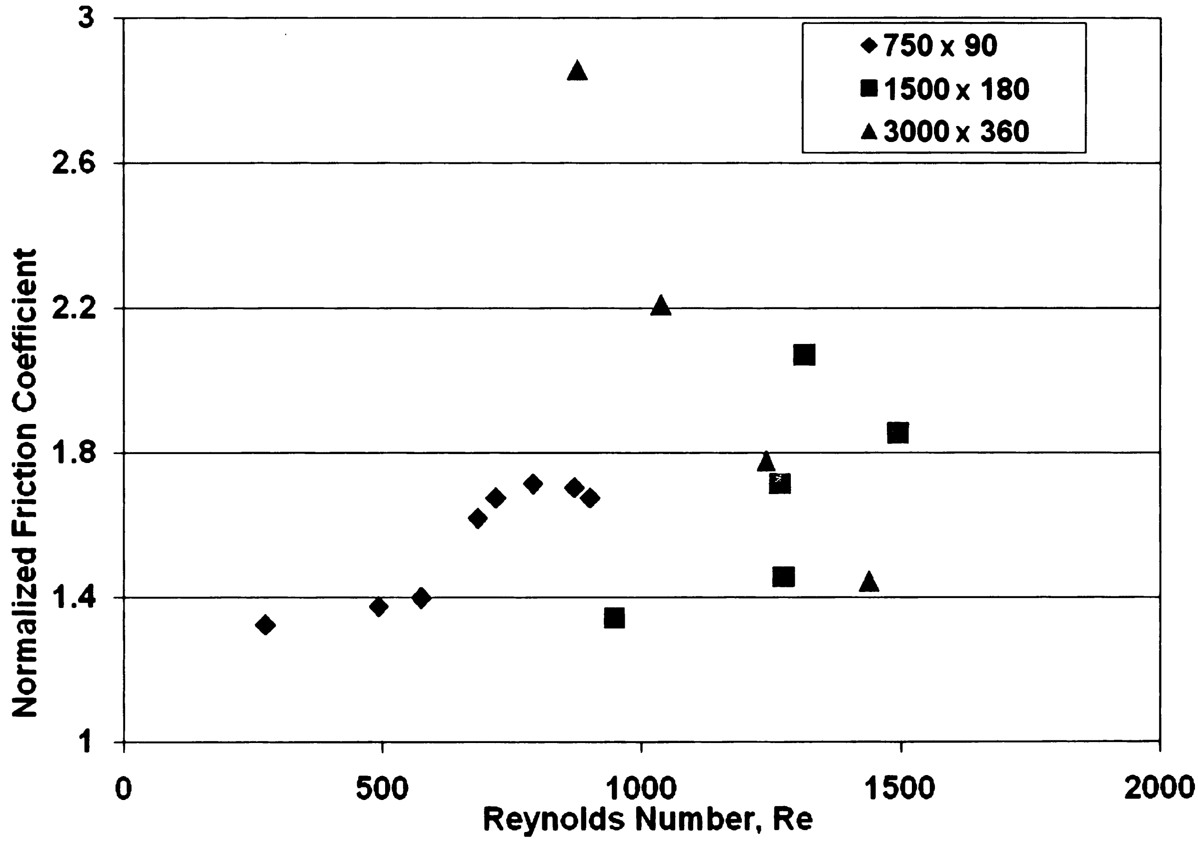

Fig 110 Plot showing Reynolds number versus the Normalized friction coefficient for three different micro channel dimensions

As shown above, the normalized coefficients show a marked deviation from the laminar flow values. Another important factor verified during the analysis was the rarefaction effect occurring during flow in micro channel. A considerable change in density is observed due to the formation of viscous boundary layers during the gaseous flow in micro channels. This fall in density due to viscous dissipation is also termed as the rarefaction effect. Figure 7 verifies the viscous dissipation and rarefaction studies previously under taken [32].

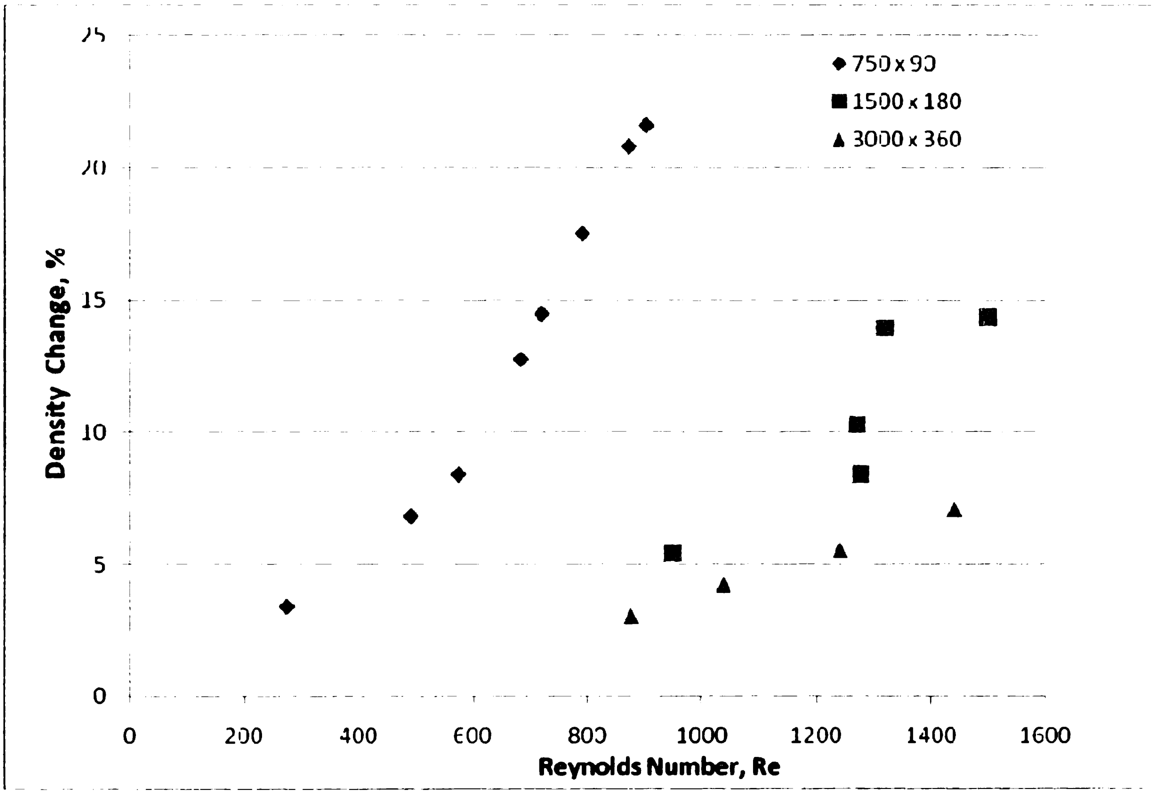

Fig 111 Plot showing the percentage of density change for different channel lengths and for different Re

Friction factor results were verified by previous experimental findings. We find comparable variations of the laminar friction coefficients for a given pressure difference compared to the macro scale theoretical predictions [30]. The results also confirm the micro scale effects in low aspect ratio microchannels, however further work is required to identify and quantify these effects. Another important factor the 'initial length effect' plays a very important role for the flow in micro scale.

Further work will deal with this aspect where it is shown that flow is not fully developed yet as the micro channel length is about 5 -8 % of the fully developed channel flow length. This is true for most micro channel flows. Because of the greater pressure losses in such a case in comparison with the "normal" laminar flow the normalized friction coefficient calculated for the full length must be obtained greater then theoretical ($C^*>1$) and this has been verified by our findings above.

CHAPTER 8 CONCLUSION

The area of power MEMS has been in considerable focus in the past decade as research groups around the world work towards developing ideas for generating power at the micro level. This work has been an attempt to present one such idea and the lays down a first ever design approach for an internal combustion wave disc engine. Using the unsteady flow and pressure exchange principles, an idea for an engine was presented and explained.

This work has discussed and covered the following:

- The principle of operation of a wave disc engine has been extensively discussed. Wave patterns and state plane diagrams have been presented for this model. A linear gas dynamic model using the powerful technique of method of characteristics has been developed, and also the governing equations have been shown. This work also discusses the assumptions for such approach and the simplifications to develop a preliminary model. The observations have been discussed and presented.

- Numerical simulations of a unsteady flow periodic machine, wave rotor were successfully performed. The results were used as a comparison for a 1 D algebraic code developed by fellow researchers. Porting design were calculated and verified using these two simulations and they are now manufactured as a part of the wave rotor test rig. Techniques employed for performing these simulations will be used to model the wave disc engine. Further work has been suggested as to how to improve the numerical methods and the possible challenges while modeling the wave disc with internal combustion.

- Micro combustion inside a micro channel could be the biggest challenge so far. Thermal, fluidic and combustion aspects of a micro scaled combustion is discussed and presented. Expected problems along with the available solutions are discussed.

- A preliminary analytical model analytical model for the wave disc engine has been made as a 1 D algebraic code and was run for a wide range of post combustion temperatures and pressures. Its affect on the design parameters like the induced flow velocities after all the expansion and compression wave, and also the behavior or the gas air interface was studied and shown. Interesting observations were made regarding the affect of post combustion temperatures and pressures and also for a 20 mm channel length the interfaces were calculated for a wide range of temperatures. This could be used to develop the first ever porting design for the wave disc engine. Several different disc design were shown from the available literature.

- Experimental work on microfluidic behavior was conducted at the University of Technology, Warsaw, Poland. Four different channel lengths were machined in a silicon wafer and friction factors were computed for all four of them using a simple volume flow rate measuring technique. The results showed good comparison to the available data in the literature. Change of density or rarefaction of the gas was also seen and plotted.

Using the presented work, a more sophisticated model of the Internal combustion wave disc engine will be developed and then eventually manufactured and tested.

References:

1. Epstein A. H, *"Millimeter-Scale, Micro-Electro-Mechanical Systems Gas Turbine Engines",* Journal of Engineering for Gas Turbines and Power, April 2004, Vol. 126

2. Epstein A. H, Jacobson S. A, Protz J. M, Fréchette L. G, *"Shirtbutton-sized gas turbines: the engineering challenges of micro high speed rotating machinery",* Proceedings of the 8th Int'l Symposium on Transport Phenomena and Dynamics of Rotating Machinery (ISROMAC'8), Honolulu, Hawaii, January 2000

3. Epstein A. H, *"Micro Turbine engines for soldier power",* Presentation, The Defense Science and Technology Seminar - Future Warrior Systems, October 2000

4. Epstein A. H, Jacobson S, Senturia S. D, *"Power MEMS and Micro Engines",* Proceedings of IEEE Transducers '97 Conference, Chicago, IL, June 1997

5. Berchtold, M., *"The Comprex Diesel Supercharger"*, Proceedings of SAE Summer Meeting, 1958

6. Akbari, P., Nalim, M.R., and Müller. N., *"A Review of Wave Rotor Technology and its Applications"*, Proceedings of 2004 ASME International Mechanical Engineering Congress & Exposition, 2004

7. Kentfield, J. A. C., *"Nonsteady, One-Dimensional, Internal, Compressible Flows",* Oxford University Press, Oxford, 1993

8. Iancu, F., *"Integration of a wave rotor to an ultra micro gas turbine (UμGT)"*, Doctoral Dissertation, Department of Mechanical Engineering, Michigan State University, 2005

9. Iancu F., Piechna, J., Dempsey E., Müller N.,*" Ultra-Micro wave rotor investigations",* PowerMEMS 2005 - 5th International Workshop on Micro and Nanotechnology for Power Generation and Energy Conversion Applications, Tokyo, Nov 2005, pp 93-96

10. Frechette, L. G., "*Development of a Microfabricated Silicon Motor-Driven Compression System,*" Ph.D. Dissertation, Mechanical Engineering, Massachusetts Institute of Technology, Cambridge, MA, 2000

11. Piechna, J. R., *"Feasibility study of the wave disk micro-engine operation"*, Journal of Micromechanics and Micro engineering, Vol. 16, S270–S281, 2006
12. Akbari, P., *"Performance prediction and preliminary design of wave rotors enhancing gas turbine cycles"*, Doctoral Dissertation, Department of Mechanical Engineering, Michigan State University, 2004

13. Shapiro, A. H., *"The Dynamics and Thermodynamics of Compressible Fluid Flow"*, the Ronald Press Comp., New York 1953

14. Piechna, J.," *Wave Machines, Models and Numerical Simulation"*, Prace Naukowe, Mechanika, z.205, ISSN 0137-2335, Oficyna Wydawnicza Politechniki Warszawskiej, Warszawa, 2005

15. Fernandez-Pello, A. C.," *Micro-Power Generation Using Combustion: Issues and Approaches"*, Prepared for presentation as a Topical Review at the Twenty-Ninth International Symposium on Combustion, Sapporo, Japan, 2002

16. Lee, S., Nelson, D., Svrcek, M., Edwards, C.F. and Bowman, C.T. "*Mesoscale Burner Arrays for Gas Turbine Reheat Applications"*, 2002 Spring Meeting, WSS/CI, San Diego, CA, 2002

17. Hetsroni, G., Mosyak, A. and Segal, Z., *"Two Phase Flow in Microchannels"*, Proceedings of the 2001 ASME IMECE, New York, NY, 2001

18. Rajan, N., Mehregany, M., Zorman, C.A., Stefanescu, S., Kicher, T.P. *"Fabrication and testing of micromachined silicon carbide and nickel fuel atomizers for gas turbine engines"*, J. Microelectromechanical Systems, 8, IEEE, September, 1999

19. Kyritsis, D.C., Guerrero-Arias, I., Roychoudhury, S. and Gomez, A. *"Mesoscale Power Generation by a Catalytic Combustor using Electrosprayed Liquid Hydrocarbons"*, Proceedings of the Twenty-Ninth International Symposium on Combustion, Sapporo, Japan, 2002

20. Lowe, H. et al. ,*"Micromixing Technology"*, IMRET 4: 4th International Conference on Microreaction Technology, AIChE Meeting, Atlanta, GA, 2000

21. Zahn, J.D., Deshmukh, A.A., Papavasiliou, A. P., Pisano, A.P.,and Liepmann, D., *"An Integrated Microfluidic Device for the Continuous Sampling and Analysis of Biological Fluids"*, Proceedings of the 2001 ASME - IMECE, , New York, N.Y. 2001

22. Weinberg, F. Fifteenth Symposium (International) on Combustion, The Combustion Institute, 1975

23. Jones, A.R., Lloyd, S.A., and Weinberg, F.J., Proceedings Royal Society (London) A, 360, 97-115, 1978

24. Lloyd, S.A., and Weinberg, F.J., Nature, 251, 47-49, 1974

25. Sirignano, W.A., Pham, T.K. and Dunn-Rankin, *"Miniature Scale Liquid Fuel Film Combustor"*, Proceedings of the Twenty-Ninth International Symposium on Combustion, Sapporo, Japan, July 21-26, 2002

26. Zhang, C. Najafi, K., Bernal, L.P., Washabaugh, P.D., *"An Integrated Combustor-Thermoelectric Micro Power Generator",* 11th Int. Conference on Solid State Sensors & Actuators, Munich, Germany, June 10-14, 2001

27. Lewis, Jr., D.H. Janson, S.W., Cohen, R.B. and Antonsson, E.K., Sensors and Actuators, Physical, 80(2), 143-154, 2000

28. Pohorelsky. L, Müller. N, Sane. P, "*Wave Rotor Design Procedure for Gas Turbine Enhancement*", Draft GT-2008-51354, Turbo Expo, Berlin Germany, 2008

29. Wu. P., "*Measurement of friction factors for the flow of gases in very fine channels used for micro miniature Joule-Thomson refrigerators*", Cryogenics, No.5, pp 273-277, 1983

30. Papautsky,I, *"A Review of Laminar Single-Phase Flow in Microchannels"*, ASME International Mechanical Engineering Congress and Exposition, New York, NY. 2001

31. White, F, "*Fluid Mechanics*", McgrawHill

32. Arkilic, E. B., *"Gaseous Slip Flow in Long Microchannels."*, Journal of Microelectromechanical Systems 6(2): 167-178, 1998